Bedforms on the submarine flanks of insular volcanoes: New insights gained from high resolution seafloor surveys

Published Version:
Casalbore, D., Clare, M.A., Pope, E.L., Quartau, R., Bosman, A., Chiocci, F.L., et al. (2021). Bedforms on the submarine flanks of insular volcanoes: New insights gained from high resolution seafloor surveys. SEDIMENTOLOGY, 68(4), 1400-1438 [10.1111/sed.12725].

Availability:
This version is available at: https://hdl.handle.net/11585/821228 since: 2024-05-21

Published:
DOI: http://doi.org/10.1111/sed.12725

Bedforms on the submarine flanks of insular volcanoes: new insights gained from high resolution seafloor surveys

D. Casalbore[1], M. Clare[2], Ed L. Pope[3], R. Quartau[4,5], A. Bosman[1], F.L. Chiocci[6], C. Romagnoli[7], R. Santos[4,5]

[1] Institute of Environmental Geology and Geo-Engineering, Italian National Research Council (IGAG-CNR), Italy

[2] National Oceanography Centre, University of Southampton, Waterfront Campus, Southampton SO14 3ZH, UK

[3]Department of Geography, Durham University, Lower Mountjoy, South Road, Durham, DH1 3LE, UK.

[4] Instituto Hidrográfico, Lisboa, Portugal

[5] Instituto Dom Luiz, Lisboa, Portugal

[6] Dipartimento Scienze della Terra, Sapienza University of Rome, Rome, Italy

[7] Dipartimento Scienze Biologiche, Geologiche e Ambientali, University of Bologna P.za Porta S. Donato 1, 40126, Bologna, Italy

Corresponding author: Daniele Casalbore, daniele.casalbore@uniroma1.it

ABSTRACT

A comparative analysis of bedform fields along the submarine flanks of insular volcanoes, characterized by different morpho-structural settings, volcanic and meteo-marine regimes (Madeira,Vanuatu, Kermadec, Bismark and Aeolian Archipelago), is presented here to provide insights on the size distribution and genesis of such bedforms. Two main types of bedforms are recognized according to their size, location and preconditioning/triggering processes. Small-scale bedforms have wavelengths of 10s-100s of meters and wave heights of meters. Because of their small-size, they are typically not recognizable at depths greater than 400 m from vessel-mounted bathymetric surveys. However, few examples of small-scale bedforms are reported from upper volcanic flanks, where steep gradients commonly hinder their formation. Their recognition is mostly limited to the thalweg of shallow and flat-bottomed channels that carve the insular shelf on slope gradients < 15°. Small-scale bedforms are related to erosional-depositional processes due to sedimentary gravity flows that are often the result of a cascading effect between volcanic and non-volcanic processes (sudden flood discharges, retrogressive landslides). Large-scale bedforms occur at all water depths, having wavelengths of 100s/1000s of meters and wave heights up to few 100s of meters. The origin of large bedforms is more difficult to ascertain, especially if only bathymetric data are available. Some diagnostic criteria are presented to distinguish between bedforms associated with landslide deposits and the ones associated with density currents. In this latter case, relevant sediment sources and slope gradients are key factors for bedform development. Erosional-depositional bedforms are typically related to eruption-fed density flows formed during large caldera collapses or to large turbidite flows. Particularly, bedforms generated by turbidite flows are observed in the lower volcanic flanks, where an abrupt decrease of gradients from 20°-30° to values less than 3°-5° is present, often matching a change from confined to unconfined settings. In summary, this study provides insights to interpret bedforms in modern and ancient marine volcaniclastic settings elsewhere as well as to better assess the hazard to offshore infrastructure related to powerful turbidity flows and/or pyroclastic flows around volcanic islands.

Keywords

Sediment waves, Aeolian Arc, Kermadec Arc, Vanuatu Arc, Madeira Archipelago, multibeam bathymetry

1 INTRODUCTION

Insular volcanoes are highly dynamic environments, where the interplay between volcanic and volcanic-tectonic, and erosional-depositional processes contribute to rapidly change their morphology (Casalbore, 2018 and references therein; Ramalho et al., 2013). Offshore, volcanic activity also has a strong influence because of its potential to rapidly delivery large amounts of volcaniclastic material, thus altering 'normal' rates of sedimentation. The large amount of volcaniclastic material coupled with the steepness of volcanic island flanks promotes widespread mass-wasting processes ranging across different spatial and temporal scales (e.g. McGuire et al., 2006). This greatly contributes to enlargement of the edifice and offshore growth of insular volcaniclastic aprons (Menard, 1956; Carey, 2000).

Volcanic islands typically represent the tip of large volcanic edifices rising thousands of meters above the seafloor. Marine studies are therefore essential to fully understand the morpho-structural evolution of the edifice and the erosive-depositional processes acting across the flanks. In the last few decades our understanding of the submarine morphology of insular volcanoes has exponentially increased with the advent of modern seafloor imaging technology (e.g. Mitchell et al., 2002; Coombs et al., 2007; Boudon et al., 2007; Leat et al., 2010; Romagnoli et al., 2013a). However, with a few exceptions, their shallow water portions remain poorly surveyed (Mitchell et al., 2008; Babonneau et al., 2013; Bosman et al., 2014; Casalbore et al., 2015, 2017a; Quartau et al., 2015; Ricchi et al., 2018; Clare et al., 2018). Nonetheless, these studies have confirmed that mass-wasting processes play a key role in the morphological evolution of submarine volcanic flanks and can pose a major hazard to offshore infrastructure (e.g. subsea telecommunication cables, Carter et al., 2014; Pope et al., 2017) and coastal communities through coastal retrogressive failure and/or tsunami generation (Chiocci et al., 2008; Tappin et al., 2008; Omira et al., 2016; Chiocci and Casalbore, 2017; Williams et al., 2019). Despite most of the attention being focused on the characterization of large-scale slope failures, a suite of smaller geomorphic features associated to erosional processes have been identified along the submarine volcanic flanks, such as gullies, furrows, channels and canyons, fan-shaped deposits, scours and bedforms (Casalbore et al., 2018 and reference therein).

The recognition of widespread fields of bedforms in modern marine volcaniclastic systems at multiple locations worldwide has recently attracted the attention of marine geoscientists, as demonstrated by the growing number of studies in literature (e.g. Wynn et al., 2000; Wright et al., 2006; Hoffman et al., 2008; Masson et al., 2008; Silver et al., 2009; Gardner, 2010; Leat et al., 2010; Sisavath et al., 2011; Casalbore et al., 2014; Mazuel et al., 2016; Pope et al., 2018; Clare et al., 2019; Quartau et al., 2018; Santos et al., 2019). These bedforms can extend over tens of kilometers; indivdual bedforms having wave heights and wavelengths of 100s and 1000s of meters, respectively. These features are (at least) an order of magnitude greater than the largest volcaniclastic bedforms recognised on subaerial volcanic flanks (Pope et al., 2018 and references therein). They can result from a) seafloor deformation due to gravity driven instabilities, b) the interaction between sediment-laden gravity flows (associated with flood discharge, slope failures or eruption-fed pyroclastic flows) and the seafloor or c) a combination of both processes. Pope et al. (2018) recently presented some morphological criteria to discriminate between bedforms generated by gravity instabilities and those generated by sediment-laden gravity flows. However, this and other studies identified the requirement for high-resolution seismic datasets to prevent erroneous interpretations (Pope et al., 2018; Quartau et al., 2018). Thus, despite the growing interest in these features, the interpretation of their emplacement mechanism often remains ambiguous.

In addition to the larger scale bedforms, small-scale and crescentic bedforms with wavelengths of tens/hundreds of meters and maximum wave heights of a couple of meters have also been identified on the upper and shallower flanks of insular volcanoes (Babonneau et al., 2013; Romagnoli et al., 2012; Chiocci et al., 2013; Casalbore et al., 2017; Clare et al., 2018). Although not as widely documented, understanding how these bedforms form can provide useful insight into the transfer of material from subaerial to the deeper marine flanks of insular volcanoes, which has broad relevance for hazards assessment as well as to understand the fate of sediment in the deep-sea.

The aim of this paper is to provide a comprehensive review of bedforms found in modern marine volcanic settings. This is based on the analysis and comparison of several (published and unpublished) case-studies from volcanic edifices in a range of different geodynamic settings and characterised by different volcano-tectonic evolutions (Fig. 1). We use bathymetry data integrated (where available) with seismic profiles, side-scan sonar data and seafloor samples. For each identified bedform field, a series of morphological/morphometric parameters were extracted, including depth range, minimum and maximum slope gradients, wavelengths, wave heights, lateral extent, slope gradients, cross-section and plan view shape of their crestlines. Local boundary conditions are also summarised including morphological settings, volcanic, meteorological and oceanographic regime, and sediment sources, where these features form in order to understand the main processes responsible for their development. Through synthesis of these data, the aim of this study is: a) to perform a comparative analysis of the morphological variability and size distribution of volcaniclastic bedforms to assess whether this is controlled by the type and magnitude of preconditioning/triggering mechanisms; b) to verify if the spatial gap identified by Symons et al. (2016) between small- and large-scale sediment waves in marine settings also applies to volcaniclastic bedforms. In the conclusion, we attempt to highlight outstanding uncertainties in the understanding of bedforms in marine volcaniclastic settings and propose recommendations to fill these knowledge gaps.

2 CASE-STUDIES

We now introduce the different case studies that are discussed in this paper (Fig 1.), providing information on the geological setting of each study area and prior observations of seafloor morphology (primarily focused on bedforms).

2.1 Macauley Volcano

2.1.1 Geological setting

Macauley Island is located in the intra-oceanic Kermadec Arc (Fig. 1) and is the uppermost subaerial edifice of an active submarine stratovolcano (Wright et al., 2006; Shane and Wright, 2011; Barker et al., 2012). Onshore Macauley Island, deposits are dominated by basaltic lavas and phreatomagmatic deposits (Lloyd et al., 1996). These are overlain by the Sandy Bay Tephra Formation and younger basaltic lavas (Lloyd et al., 1996). The Sandy Bay Tephra is the only confidently known silicic activity related to this volcano and consists of a massive lithic basal unit overlain by multiple wet pyroclastic density current and surge deposits (Smith et al., 2003; Barker et al., 2012). The majority of the Macauley volcanic complex is submerged, with the submarine landscape dominated by the Macauley Caldera to the northwest of the island (Fig. 2).

2.1.2 Bedform fields

The flanks of the Macauley volcanic complex are dominated by repetitive bedforms which extend out for >20 km from the rim of Macauley Caldera in the west and >55 km to the east of the volcanic complex (Fig. 2a). These bedforms occur at depths ranging from 50 m to >3300 m (Table 1) and cover an area >1750 km^2. Due to a lack of data coverage we are unable to map their furthest extent. The range of bedform wavelengths and wave heights is 125 – 2450 m and 5 – 200 m respectively. The characteristics of the bedforms are highly variable and will subsequently be examined independently according to their perceived formative process.

Upper-flow regime bedforms

Repetitive bedforms fields (MC1 and MC2, Fig. 2) extend outwards on the southwest and northern flanks of Macauley Volcano for >25 km and cover an area of >320 km^2 and >220 km^2 respectively. On the southwest flank, bedform wavelengths decrease seaward from 1500 m to 250 m, whilst their amplitudes decrease from 140 m to 5 m. On average the northern flank is steeper (2.7° vs. 1.85°) than the southwest flank. Here, bedform wavelengths and amplitudes decrease seaward from 1650 m to 220 m and 160 m to 5 m respectively.

The bedforms of both MC1 and MC2 fields have poorly defined lateral margins and are convex in planform (Fig. 2a). In bathymetric profile the lee sides of these bedforms is often steeper and shorter than their stoss sides making the bedforms asymmetric. Although only available perpendicular to the perceived direction of flow for MC1, high-resolution seismic data also indicates that the bedforms are made up of asymmetric sediment packages (Fig 2b, c). The seismic data from MC1 shows multiple high amplitude reflectors making up chaotic facies separated from a series of thin, ordered lower amplitude reflectors by a stratigraphic unconformity (Fig. 2c). Although its strength varies, a further internal unconformity exists within the lower amplitude reflectors (Fig. 2b, c). There are >20 planar reflectors beneath this surface and >30 above (Fig. 2c). The lower set of bedform reflectors are truncated at high angles on their lee sides and this form asymmetric structures. (Fig. 2c). The upper set are more clearly developed and conform to the underlying unconformity. These reflectors have a dome-like apex and their lee sides are thin but not truncated, instead becoming unresolvable. These characteristics mean that the top set of reflectors are more symmetric in form but remain asymmetric.

On the basis of the seismic data and their morphologies, the bedforms of MC1 have been interpreted as being emplaced by poorly confined sediment density currents probably resulting from the radial collapse of an eruption column (see Pope et al., 2018 for full discussion). The bedform symmetry and architecture suggests that stoss-side deposition and lee side erosion occurred during their formation. This suggests that the bedforms migrated upstream and are therefore representative of either cyclic steps of anti-dunes. Of these, the lower set of reflectors is thought to relate to cyclic steps due to their longer wavelength and more asymmetrical form (Cartigny et al., 2011). The upper set are interpreted to be reflective of anti-dunes due to their greater symetry and apparent conformation to the underlying bedforms.

In contrast to MC1, no seismic data is available which runs perpendicular to the orientation of MC2. We are unable to definitively attribute the formation of this bedform field to a specific process. However, the morphology of the bedforms in MC2 is similar to that of MC1 (Fig. 2). we therefore envisage a similar formative process for these bedforms, i.e. eruption-fed density currents.

Mass-wasting bedforms

The repetitive bedforms fields (MC3 – 6, Fig. 2a) extend outwards to the north, east and south of the Macauley volcanic complex for >45 km. These bedforms occur at depths of between 350 m and 3300 m and cover a combined area of >545 km^2 (Table 1), extending seaward beyond our available data coverage. The wavelengths of these bedforms ranges from 125 m to 2450 m and their amplitudes range from <10 m to 200 m (Table 1). However, neither their wavelengths nor their amplitudes systematically decrease with distance from the shelf edge. The average slope gradients of MC3 – 6 are 4.89°, 3.66°, 3.34° and 3.57° respectively. These are significantly greater than the average slope gradients of bedform fields MC1 and MC2 (Fig. 2d).

Unlike bedforms in MC1 and MC2, the bedforms in MC3 – 6 have sinuous to linear or concave crestlines and are symmetrical with flat tops. The lateral margins of these bedform fields are also commonly well-defined on the upper flanks of the volcanic complex and often originate from distinct arcuate headwalls (Fig. 2a).

Although the emplacement mechanism of these bedforms is uncertain they are interpreted as likely a consequence of slope failure or creep because; 1) bedforms originating originate from distinct arcuate headwalls consistent with landslides and; 2) bedform from trains are laterally confined within valleys and absent on interfluves (Pope et al., 2018).

2.2 Zavodovski Volcano

2.2.1 Geological setting

Zavodovski Volcano is part of the South Sandwich Arc which is built on the small oceanic Sandwich plate in teh South Atlantic (Fig. 1; Larter et al., 2003; Leat et al., 2010). Zavodovski Volcano is ~11.6 km^2 and is dominated by a single volcanic cone, Mount Curry (Leat et al., 2010). Zavodovski Island is dominated by basalt and basaltic andesites (Pearce et al., 1995; Leat et al., 2003).

2.2.2 Bedform fields

The eastern flanks of Zavodovski Volcano are characterised by a series of chutes and repetitive bedforms which extend >50 km from the shelf edge (Fig. 3a). The bedform fields, Zd1 – 3, occur at depth ranges of between 160 m and >2800 m and cover an area of >850 km^2 extending eastward beyond the coverage of available bathymetry (Table 1).

Bedform fields Zd1 and Zd3 have the greatest spatial extents, 368 km^2 and >313 km^2 respectively. They also have the greatest bedform wavelengths and wave heights, but both decrease in a seaward direction. Bedform wavelengths Zd1, which has the steepest average slope gradient of the bedform fields (2.94°) decrease from 2800 m to 380 m and wave heights decrease from 144 m to 5 m (Table 1). Bedform wavelengths and wave heights in Zd3 (average slope gradient 2.78°) decrease from 2960 m to 285 m and 175 m to 24 m. Both Zd1 and Zd3 have poorly defined lateral margins. Their planform morphologies are also characterised by changes from concave to convex morphologies with increasing distance offshore (Fig. 3a). In profile, the bedforms of Zd1 and Zd3 are commonly characterised by shorter steep lee sides giving these bedforms a downslope asymmetric profile (Fig. 3b, d).

Bedform field Zd2 has contrasting characteristics with Zd1 and Zd2. It has the smallest spatial extent of the three bedform fields (186 km^2). Of the bedform fields it also has the lowest average slope gradient (1.78°) and smallest wavelength bedforms (900 – 1900 m). The wave heights of the bedforms are between Zd1 and Zd3 (8 – 164 m). Unlike Zd1 and Zd3, Zd2 has clearly defined lateral margins. On the upper slope they are confined within a gully. On the lower slope they are constrained by the bedforms of Zd1 and Zd3, which have conspicuously different wavelengths. Zd2 planform morphologies are predominantly characterised by concave morphologies. In profile, upper to mid-slope bedforms often have short stoss sides and long lee sides (Fig. 3c). Only in the lower slope are the shorter lee sides observed in Zd1 and Zd3 (Fig. 3c).

The origin of Zavodovski Volcano bedforms is difficult ascertain. All the bedform fields originate from headwalls at the shelf edge and are confined within gullies in their upper reaches. This is suggestive of a landslide/slump origin (Hampton et al., 1996). However, a number of features suggest that these bedforms can also be related to sediment density flows. First, sub-bottom profiler data perpendicular to the perceived direction of flow across Zd1 and Zd3 has shown a veneer of downslope prograding sediments containing internal reflectors (Leat et al., 2010). Second, overbank sediment deposits have been identified (Leat et al., 2010). Third, the planform morphologies of Zd1 and Zd3 are similar to those on other volcanic islands attributed to sediment density flows (see Section 4a). These bedforms may of course also be a consequence of sediment density flows and mass-wasting processes (Leat et al., 2010).

2.3 Dakataua Caldera and Kimbe Bay

2.3.1 Geological setting

Dakataua Caldera and Kimbe Bay are located on New Britain and are part of the Bismark Volcanic Arc (Fig. 1; Silver et al., 1991). Dakataua Caldera lies at the northern tip of the Willaumez Peninsula and is thought to have collapsed 1270 – 1350 years ago (Neall et al., 2008). The eruptive histories of Dakataua Caldera and Mt. Makalia, which is current located within the caldera, are dominated by andesitic lavas and ash deposits. Some porphyritic basaltic andesites and dacitic flows have also been observed (Lowder and Carmichael, 1970). In contrast to other examples in this study, Kimbe Bay is flanked by multiple volcanoes, including Witori and Mt Garbuna, and multiple small rivers which drain them (Hoffmann et al., 2008; Neall et al., 2008). Volcanic products from Witori and the surrounding volcanoes are dominated by a combination of basaltic andesite and andesite although basalts and dacites are also present (Blake and Bleeker, 1970).

2.3.2 Bedform fields

Two repetitive bedform fields extend from the northern flanks of Dakataua Caldera for ~30 km (Fig. 4a). To the northeast there is also an area of large blocks ~30 km^2 which believed to have been deposited by a previous sector collapse (Silver et al., 2009). The two bedform fields, DC1 and DC2, occur at depth ranges of between 1450 m and 2100 m and cover areas of 550 and 520 km^2 respectively (Table 1). DC1 has the lower average slope gradient (0.9° vs 1.63°). Here, bedforms decrease in wavelength and wave height with distance from the Dakataua Caldera from 3500 m to 384 m and 92 m to 5 m respectively. The bedform wavelengths and wave heights in DC2 similarly decrease from 2860 m to 820 m and 115 m to 10 m (Table 1).

Both DC1 and DC2 areas have poorly defined lateral margins. However, the bedforms fields have contrasting morphologies. Bedforms in DC1 are characterised by sinuous to linear planform morphologies (Fig. 4a). The bedforms also show no coherent pattern of asymmetry in profile (B – B', Fig. 4b) until water depths >1900 m (A – A', Fig. 4b). In contrast, bedforms in DC2 are characterised by convex planform morphologies with observed bifurcation (Fig. 4a). They also commonly exhibit asymmetry in profile with shorter steeper lee sides (Fig. 4c).

Attributing a definitive formative process for the Dakataua Caldera bedform fields is difficult as no seismic data is available for DC1 and sub-bottom profiles across DC2 failed to penetrate the seafloor (Hoffmann et al., 2008). However, sediment density flows and mass-wasting processes are suggested to both have played a role in the formation of these bedforms (Hoffmann et al., 2008; 2011). The reduction of wave height and wavelength with distance from the caldera and the downslope orientation of scour features observed in sidescan imagery are both suggestive of sediment density flow activity (Hoffmann et al., 2008; 2011). The bedform planform and profile morphologies, particularly those of DC2, also resemble bedforms thought to be related to sediment density flows (Pope et al., 2018).

The seafloor at the centre of Kimbe Bay is dominated by a field of repetitive bedforms which extends >40 km in a NNW-SSE direction (Fig. 5a). The Kimbe Bay bedforms occur between water depths of 1500 m and 2200 on an average slope gradient of 0.8°. The bedforms have wavelengths of 494 m to 3400 m and wave heights of 7 m to 92 m. The lateral margins of the Kimbe Bay bedform field is poorly defined on its northern and western edges. To the east, it is constrained by a crevice and the Kimbe Bay Escarpment (Fig. 5a). In planform the bedforms are predominantly characterised by convex morphologies and bifurcation is common (Fig. 5a). In profile, there is large variability in the symmetry of the bedforms, ranging from strongly downslope to strongly upslope asymmetry (Fig 5).

Morphologically similar to the bedforms in DC1 (Fig. 4a), the origin of the Kimbe Bay bedforms has been interpreted as a consequence of sediment density flow activity and extensional creep. Enclosed depressions are interpreted as suggestive of deformation (Hoffmann et al., 2011). However, sub-bottom profiler data shows thicker sediment packages on the upslope limbs of bedforms as well as the upslope migration of sediment packages consistent with sediment density flows (Wynn et al., 2002; Hoffmann et al., 2008; 2011). Nearby channels and plunge pools also suggest sediment density flow activity near the bedform field. It is also hypothesised that the crevice may be the site of focussed sediment density flows (Hoffmann et al., 2008). Both Dakataua and Kimbe Bay examples require additional seismic and core data is required to define the dominant process.

2.4 Aeolian Archipelago

2.4.1 Geological setting

The Aeolian archipelago is the subaerial part of a 200 km wide volcanic arc located in the Southern Tyrrhenian Sea (Fig. 1 and Fig. 1 ESM). Aeolian volcanism is considered to be subduction related and is associated with rifting processes developing within the arc collision zone (Ventura, 2013 and references therein). Volcanic activity ranges from effusive to explosive (from Strombolian to Plinian). Explosive eruptive activity has occurred on Salina and Panarea during the Late-Quaternary (Lucchi et al., 2013). Whilst Stromboli is characterised by persistent Strombolian activity (Rosi et al., 2000), Vulcano and Lipari are characterised by by historical eruptions (AD1888-1890 vulcanian-type eruption and AD1230 obsidian flows, respectively).

2.4.2 Bedforms

Large-scale bedforms have previously been presented in Casalbore et al. (2014). There morphological/sedimentological characteristics are therefore summarised in Table 1 and briefly presented in the ESM. Small-scale bedforms are described in detail below.

Stromboli

Small-scale bedforms (Str 4 in Fig. 1 ESM) are found at depths of 30 – 170 m within a 600 m wide flat-bottomed channel carving the saddle between Stromboli and Strombolicchio edifices (Piscità Channel, Fig. 6a). Bedforms have wavelengths of 20 – 86 m and wave heights of 1 – 5 m. Their crestlines are arcuate to crescentic and are generally downslope asymmetric in cross section with steep (up to 28°) less sides (Fig. 6). Bedform size tends to increase downslope in spite of the superposition of smaller bedforms on large ones, which also indicates the occurrence of multiple sediment gravity flows (Fig. 6).

Repeat bathymetric measurements from 2002 – 2015 (Figs. 6b and c) indicate significant morphological change occurred in the channel during or just after the main eruptive crisis affecting Stromboli in 2002, 2007 and 2014. Changes to the bathymetry show an overall upslope migration of the bedforms (Casalbore et al., 2017b), allowing us to interpret these bedforms as upper-flow regime bedforms, similar to those small-scale and crescentic-shaped bedforms identified in non-volcanic settings (e.g. Clare et al., 2016). Small, fresh-looking landslide scars were also observed at the head of the Piscità Channel, affecting the littoral wedge up to depths of 5 m, less than 100 m from the coastline (Fig. 6a).

The active morphologic seabed behaviour can be related to increased longshore transport after the major eruptive crisis when subaerial lava flows entered the sea and large amounts of volcaniclastic debris was produced at SdF (Romagnoli et al., 2006). This increased sedimentary input is intercepted by the Piscità channel, and likely acted as the main preconditioning factor for the development of small gravity instabilities and resulting sediment-laden flows. These flows were likely triggered by seismic events during eruptive crisis or by cyclic loading associated with severe storms which periodically affect Stromboli.

Salina

Small-scale bedforms have been identified along the north and east flanks of Salina (Sal1 and Sal2, respectively in Fig. 1ESM). The northern bedform field is located within a 1 km wide, flat-bottomed channel (North Salina Channel, Fig. 7a), whose headwall incises the outer edge of the insular shelf. Here, from 285 – 677 m, arcuate to crescent-shaped bedforms are observed with wavelengths of 44 – 215 m and wave heights of 1 – 6 m. In cross-section, the bedforms are mostly characterised by downslope asymmetry, with steep lee sides (up to 20°, Fig. 7). Bedform size generally increases downslope. In contrast to bedforms in the Piscità Channel, bedforms in the North Salina Channel show little evidence of morphological change over the 11 years (Casalbore et al., 2017b). Grab samples from the North Salina Channel recovered coarse-grained sand in the lower part of the deposit (locally with gravel), transitioning to find-sand or sandy silt to silty mud in the upper part (Casalbore et al., 2013). Based on this evidence, the origin of these bedforms could be related to sediment gravity flows generated at the shelf edge where fresh-looking scars are present. However, the size of the bedforms and the present-day disconnection between the channel and active coastal dynamics, as well as the lack of morphological change over the period of observation could suggest that these bedforms were formed when sea-level was lower and thus greater connectivity between subaerial and submarine processes. Specifically, the frequency and intensity of bedform generating processes might have been greater at the time of the lower Pollara explosive eruptions (15.6 cal ka; Lucchi et al., 2013), when a large volume of pyroclastic material was discharged into the sea.

The eastern bedform fields offshore Salina are the result of the coalescence of several coaxial trains of bedforms associated with different channels. Here, the channel headwalls are located a few tens of meters from the coastline at water depths of 5 – 10 m (Fig. 8). These arcuate to crescentic-shaped bedforms are found at depth of 45 – 430 m with wavelengths of 12 – 153 m and wave heights of 0.2 – 5.4 m. They are downslope asymmetric with short and steep (up to 30°) lee sides (Fig. 8). Trains of bedforms begin within narrow and shallow channels as well as fan-shaped features, merging downslope in a wide, flat-bottomed channel (Fig. 8). A progressive increase of wavelength and lateral extent with depth is observed. This is associated with a decrease in slope gradient and channel enlargement, or the development of fan-shaped features. Compared to previous examples, wave height shows a more scattered distribution, with a general increase in correspondence with the narrow and confined channelized features. Superimposition of different trains of bedforms with different sizes is also observed. Grab samples from this bedform field mainly recovered fin/medium sand on the upper part of the submarine flank, passing downslope to a silty sand. The genesis of these bedforms is likely to be related to sediment gravity flows originating from the channel heads which result from channel interception of littoral drift and cyclic loading from storm waves. These channels are also located offshore a subaerial drainage system which has developed on the volcaniclastic Monte Fossa della Felci units. This drainage system may have funnelled volcaniclastic debris into the sea, contributing to the dismantling of the insular shelf, and thus promoting the connection between subaerial and submarine drainage systems proposed by Romagnoli et al. (2018).

Vulcano

Small-scale bedforms were identified on the northwest and northeast of Vulcano (Vul 2 and 3, respectively in Fig. 1 ESM). The northwest bedform field form a coaxial train along the thalweg of flat-bottomed channels between 200 and 450 m (where data resolution strongly decreases) on slope gradients of 3° to 9° (Fig. 9a). Bedforms have wavelengths and wave heights of 30 – 106 m and 1.2 – 3.8 m respectively. They are mostly downslope asymmetric with steep lee sides (Fig. 9). Bedform size generally increases downslope, but strongly depends on channel shape. These bedforms were likely produced by sediment gravity flows associated with retrogressive erosion of the channel flanks and headwall where large amounts of volcaniclastic material is stored (Romagnoli et al., 2013b).

Offshore northeast Vulcano, bedforms are present in a few narrow gullies draining the submarine part of La Fossa Caldera from 70 – 200 m on slopes of 7° to 9° (Fig. 9a). These crescent-shaped bedforms have wavelengths of 21 – 62 m and wave heights of 0.7 – 2.8 m. They are most downslope asymmetric in cross-section with steeper lee sides (Fig. 9). Downslope, larger bedforms are recognisable on the Baia di Levante fan between 500 and 800 m on slope gradient of 5° to 7°. These bedforms have wavelengths of 36 – 92 m and wave heights of 1 – 4 m. They are downslope asymmetric in cross section with sinuous crestlines in plan-view. In both cases, bedforms are associated with sediment gravity flows dismantling the La Fossa Caldera infill leading to the formation of the large Baia di Levante volcaniclastic fan downslope (Romagnoli et al., 2012). Although La Fossa Caldera has been considered as the likely source area of recurrent, energetic hydromagmatic explosion between 80 and 8 ka (Lucchi et al., 2008, 2013), pyroclastic flows are not thought to be related to bedform development.

2.5 Tanna Island

2.5.1 Geological setting

Tanna Island is located in the Vanuatu volcanic arc in the southwest Pacific (Fig. 1). Volcanism on Tanna Island is currently focussed on Mount Yasur, which is a scoria cone formed from repeated strombolian- and vulcanian-style eruptions that occur every few minutes (Nairn et al., 1988; Merle et al., 2013). Yasur has been fed by a steady state magma reservoir for at least the (Nairn et al., 1988; Merle et al., 2013). Yasur has been fed by a steady state magma reservoir for at least the last 600 years (Nairn et al., 1988; Merle et al., 2013; Firth et al., 2014); however, there is evidence for at least two major ignimbrite-forming eruptions that occurred approximately 43 ka and 3-8 ka (Firth et al., 2015) and formed the complex Siwi ring fracture which extends offshore; although its expression is locally obscured by more recent seafloor sediment transport (Clare et al., 2018). Tanna Island is extremely tectonically active. Shallow magma intrusion drives significant post-caldera uplift, with uplift rates of 156 mm/year calculated over the last 1000 years (Chen et al., 1995). Two earthquake events in AD 1878 caused up to 12 m of vertical co-seismic uplift of the coastline (Clare et al., 2018). While these volcanically-driven ground movements are very likely to influence offshore sediment transport, the main triggers attributed to recent offshore turbidity currents are related to non-volcanic events, including elevated sediment discharges from rivers and the coastline during tropical cyclones, and a volcanic lake outburst flood that occurred in AD 2000 (Clare et al., 2018).

2.5.2 Bedform fields

The area surveyed offshore Tanna shows an abundance of asymmetric bedforms, which are typically crescentic in planform, with low angle upstream stoss sides and steeper angle downstream lee sides (Fig. 10). Four bedform fields are defined. First, is a broadly channelized field of bedforms (Vn1) that initiates close to the offshore outflow of the Siwi River. Here, bedform trains are of low amplitude (1-2 m) and wavelength (10-15 m); however, where bedform trains and channels coalesce into broader fairways away from the source, they tend to increase in size (2-8 m amplitude, up to 150 m wavelength). Stoss-sides are generally 1-3 degrees, with lee-sides of up to 25 degrees. The bedform field generally broadens from 10 m wide near the Siwi River outflow (20 m water depth), to 400 m on an unconfined slope at 250 m water depth. Bedform size does not solely relate to distance from source, however. Zones of larger bedforms with a higher wavelength to amplitude ratio than the rest of the surveyed area are found immediately seaward of the of the submerged ring fracture (i.e. past caldera collapse). This underlying structural influence creates a locally steeper slope, which may promote erosion and ignition of flows (thus capable of creating larger bedforms). Grain size analysis from crescentic bedforms in the submarine bedform field offshore from Siwi River reveals a very similar distribution to samples from the river (mean grain size of c.400 um), with clear bimodality at the most proximal location, becoming progressively finer (mean grain size of c.100 um) offshore (Clare et al., 2018). Transmitted light and scanning electron microscopy show that sediment is dominantly comprised of basaltic lithics with a small component of volcanic glass. Small amounts of carbonate and coralline debris are incorporated further offshore. No sampling was possible in the other bedform fields, hence is not reported. The second bedform field (Vn2), is headed by steep linear gullies that feed into a sinuous channel, which becomes deflected by a remnant block (from the last phase of caldera collapse). Here, bedforms reach 2-5 m amplitude, with wavelengths of 20-80 m. Stoss-sides are generally 1-3 degrees, with lee-sides of up to 30 degrees. The third bedform field (Vn3), is represented by a linear channel (also fed by gullies) with bedforms of similar scale to Vn2. Finally, the fourth bedform field (Vn4), occurs down-stream of a carbonate platform fringed by reefs, and includes a broad (up to 200 m-wide) linear channel. Bedforms within Vn4 are up to 6 m in amplitude with wavelengths of up to 60 m.

2.6 Madeira Archipelago

2.6.1 Geological setting

The Madeira Archipelago is located in the northeast Atlantic, ~1000 km southwest of the Iberian Peninsula (Fig. 1). It comprises the islands of Madeira (737 km^2), Porto Santo (42 km2), Desertas (13 km^2) and Selvagens (2.78 km^2). Although administratively included in Madeira Archipelago, the

Selvagens Islands are located ~280 km south of Madeira Island, and ~165 km north of the Canary Islands and appear to be related to the Canary hotpsot track volcanism (Geldmacher et al., 2001). Madeira is the youngest island, with volcanism spanning 7 Ma to the Holocene (Geldmacher et al., 2000; Ramalho et al., 2015). It is an elongated shield volcano. The island (870 km^2) is highly dissected by subaerial erosion, but still with ∼25% above 1000 m. Annually, Maderia receives 600 mm of precipitation at sea level and 3000 mm in the highest elevation. Unevenly distributed throughout the year, intense rainfall events make the island very prone to flash floods and related subaerial landslides (Baioni, 2011).

The Desertas Islands are the subaerial expression of a 50 km-long NNW-SSE trending arm with ~5 km of average width. These islands (from north to south: Ilhéu Chão, Deserta Grande and Bugio) were heavily destroyed by wave erosion and landsliding, featuring now only 22 km of subaerial exposure, <1 km in width and < 477 m in height. The volcanism of Desertas shows many similarities with Madeira's, although its volcanic activity stopped 1.9 Ma ago (Schwarz et al., 2005).

Porto Santo is separated from the Madeira-Desertas rift system by a 30 km wide and 2500 m deep channel. It is much older than Madeira and Desertas, with volcanic activity confined to 14-10 Ma (Schmidt and Schmincke, 2002). Surrounded by a wide shelf (up to 14 km), it has experienced significant erosion and now lies below 517 m. It receives <400 mm of precipitation on average and has an ephemeral subaerial drainage system that only flows after heavy rainfall.

The Selvagens consist of two groups of islands and islets, separated by ∼15 km (Santos et al., 2019). The northeast group consists of two small islets and Selvagem Grande. The southwest groups is composed of Selvagem Pequena and numerous small islets. Selvagem Grande is ∼2.41 km^2, and is basically a cliff-bounded plateau, 80 to 100 m in elevation. Selvagem Pequena is ∼0.2 km^2 (0.37 km^2 including the islets), with an average height of 10 m. The subaerial history of Selvagem Grande comprises three volcanic stages and two erosional stages to see level (that resulted in submergence and deposition of marine sediments), spanning a period of volcanic activity of 26 – 3 Ma (Geldmacher et al., 2001). The subaerial part of the Selvagem Pequena is dominantly composed of rocks from the older volcanic stages, dated ~29 Ma (Geldmacher et al., 2001).

2.6.2 Bedform fields

East of Desertas

A large bedform field (MA1 in Figs. 11 and 2 ESM) with ~1900 km^2, occurs east of Desertas Islands at 2900 – 4300 m wd (Quartau et al., 2018). The bedforms are sinuous in plan-view and can be divided into two areas by their morphological setting. The southern field (limited by the black lines in Fig. 11 and characterised by profiles DS1 and DS2) occurs offshore a 11 km long shelf edge scar (Fig. 11). It is composed of bedforms with wave heights of 5 – 31 m and wavelengths of 746 – 3014 m. In cross-section, bedforms change from asymmetric to upslope asymmetric. The northern field occurs at the end of channels which drain the eastern submarine slopes of Desertas (DS3 – DS4, Fig. 11). Here, bedforms are larger with wave heights and wavelengths of 8 – 47 m and 1016 – 4352 m, respectively. Cross-sectional profiles are similar to the southern field bedforms. In general, bedforms of MA1 tend to increase in wavelength and decrease in wave height with depth.

The bedforms of MA1 were considered by Quartau et al. (2018) to be the result of unconfined sediment density flows that were initially constrained within channels but became unconfined downslope where the drainage systems open, spreading sediments over wide areas. The end of the channels also coincides with a large gradient change from 20 – 30° to <5°. The gradient change and dispersion are thought to result in hydraulic jumps resulting in the formation of the bedforms. In contrast, the southern bedform field does not have well-defined lateral margins (Fig. 11) but appear to originate from a distinct arcuate headwall scar formed by one or multiple landslides. These bedforms could therefore be compressional feature of the debris avalanche deposit. However, the coincidence large seafloor gradient change, suggests that these could also be formed by sediment gravity flows. These flows probably result from recurrent erosion of the headwall scar and remobilisation of deposited shelf sediments.

South of Porto Santo

A small (~150 km²) bedform field (MA2, Fig. 11; Fig. 2 ESM) occurs south of Porto Santo Island at 3250 – 4000 m wd, offshore a 13 km-long shelf edge scar (Fig. 11). The bedform trains have wave heights of 19 – 124 m and wavelengths of 1369 – 2322 m. They are sinuous in plan-view and upslope asymmetric to symmetric in cross-section (PS1, Fig. 12). Given the well-defined lateral margins and the distinct arcuate headwall scar, these bedforms appear to originate from a big landslide. However, it is again more likely that they originate from several small failures producing sediment density flows that decelerate as they meet the significant seafloor gradient change (~30° – 20° to <5°) (Quartau et al., 2018). The irregular surface formed by the debris avalanche deposits could also have promoted the development of bedforms (Quartau et al., 2018).

North of Porto Santo

A large (~1500 km²) bedform field (MA3, Fig.12 and Fig. 2 ESM), occurs north of Porto Santo Island at 2500 – 3600 m. The bedform field can be divided into to two areas according to their setting. The more eastern field, confined by the black lines (Fig. 12), with a fan shape, and one with an indistinct shape. The fan-shaped field is formed by a series of channels and interfluves that originate from an arcuate headwall scar at the shelf edge of Porto Santo and show a divergent geometry. The bedforms inside the channels are crescentic downslope in plan-view and change between upslope asymmetric and symmetric in cross-section (some are downslope asymmetric). They are 2 – 16 m high with wavelengths of 228 – 983 m. The interfluve bedforms are crescentic upslope in plan-view and change between upslope asymmetric, downslope asymmetric and symmetric in cross-section. They are significantly larger than those in the channels with wave heights of 4 – 35 m and wavelengths of 706 – 1248 m. West of the fan-shaped field, the bedforms occur mostly north of a 25 km-long submarine ridge that originates on the northwest tip of the Porto Santo shelf edge. These bedforms are less, defined and more irregular in plan-view. However, their cross-section shape and sizes are very similar to those on the interfluves.

Assigning an emplacement mechanism is difficult, however, the fan shape and arcuate scar upslope suggests that the interfluves of the eastern area of MA3 could be compressional features of debris avalanche deposits. The bedforms inside the channels resulting from sediment density flows that are eroding older avalanche deposits. These events likely originate from small failures of the headwall scar which decelerate when the experience large changes in gradient. The western irregular bedforms are more difficult to explain as there are no channels upslope. The only source appears to be the volcanic ridge, which shows well developed cones up to 2000 m in diameter. It is known that relatively intense explosive eruptions can occur at depth <500 m and even below (Cas and Simmons, 2018; Chadwick et al., 2008), producing pyroclastic flows, which potential could be responsible for the bedforms.

South of Selvagens

A small bedform field (SEL1 in Fig. 13 and 2 ESM) with ~180 km2, occurs south of Selvagens at 2300-3400 m depth. The bedform field can be divided in two areas according to their morphologic setting (see profiles SV1 and SV2 in Fig. 13). A more eastern and deeper one that starts at ~3000 m depth and a more western and shallower one that starts at 2300 m depth. The eastern one occurs at the end of channels that start as headwall scars at the shelf edge of Selvagem Grande and dissect the submarine slopes of island. These bedforms are 1-17 m in height and 345-1542 in wavelength, are sinuous in plan-view and change between upslope asymmetric and symmetric in cross-section. The more western bedforms are similar in plan- and cross-section views but are significantly larger, 2-42 m in height and 345-1542 in wavelength. These occur on the base of the volcanic ridge linking Selvagem Grande to Selvagem Pequena, also at the end of smaller channels that dissect the slopes of the ridge. On both cases the bedforms start at the transition from high-slope gradients to gradients smaller than 5º. Thus, the most likely explanation for the formation of these bedforms is the presence of unconfined sediment density flows, or in the case of the more western field, pyroclastic flows from the volcanic ridge, which occurs at depths <500 m.

North of Selvagens

Two Bedform fields (SEL2 and 3 in Fig. 13) with areas of 20 km^2 and 25 km^2 at water depths of 2800 – 3400 m occur north of Selvagens at the end of channels which originate at the shelf edge of Selvagem Grande. These bedforms begin where slope gradients significantly decrease (30° – 20° to <5°). The bedforms are similar in size (see profiles SV3 and SV4 in Fig. 13), but those of SEL2 are slightly smaller (2-16 m in height and 339-772 in wavelength) than those of SEL3 (4-35 m in height and 439-1026 in wavelength). The shapes are also similar, changing between upslope asymmetric and symmetric in cross-section and crescentic downslope forms in plan-view (although in SEL3 are also crescentic upslope ones). The bedforms were likely formed by sediment density flows that spread sediments at the end of channels, where there is the big gradient decrease.

Southwest of Selvagens

A bedform field (SEL4 in Fig. 13) occurs at a different setting than the previous ones, and slightly deeper (3300-3600 m). The base of the submarine slopes of Selvagens are marked by several scour features, with rectangular or u-shaped in headwall scars in cross-section which are 3 – 30 km wide, 10 – 20 km long and 40 – 100 m deep (Santos et al., 2018). The bedform field, 50 km^2, occurs at depths of 3300 – 3600 m immediately offshore of the biggest scour. The bedforms have wave heights of 1 – 10 m and wavelengths of 198 – 784 m, respectively and are dominantly symmetric in cross-section. They are not distinguishable in plan-view due to poor resolution bathymetry. Sediment density flows are thought to generate the scours and subsequent bedforms as they experience a significant drop in gradient (from 3° to 0.5°) at the end of the submarine channel down which they were flowing (Santos et al., 2019).

3 DISCUSSION

The previous section has shown bedforms to be widespread in modern marine volcaniclastic settings and display large variability in their size, morphology and location. The recognized bedforms are characterized by crescent-shaped or sinuous crestlines that are roughly aligned perpendicular to the regional slope gradient, indicating that gravity-driven processes play a dominant role in their development. Their genesis has been related to two main kind of processes: cyclic erosional-depositional processes associated with sediment-laden gravity/eruption-fed pyroclastic flows and the seafloor displacement due to slope failures. A combination of both processes is also possible (see Hoffman et al., 2008). The rough morphology created by landslide deposits may enhance the successive development of erosional-depositional bedforms as sediment density flows cross those areas. The main triggering mechanisms for the recognized bedforms are presented in Table 2 and a discussion on the diagnostic criteria useful to distinguish between these two types of the bedforms is presented in the final sub-section 3.2.

As already mentioned in the introduction, this paper now mainly focuses on bedforms emplaced by erosional-depositional processes and will not discuss every kind of seafloor feature.

3.1 Morphology and size of the bedforms in modern marine volcaniclastic setting: is there a real distinction between small- and large-scale bedforms?

We integrate our data with other examples of submarine volcanic bedforms in the literature in order to make a general distinction between shallow (depth <400 m), small-scale bedforms (wavelengths of tens/hundreds of meters and wave heights of few/some meters) and deep (depth >800 m), large-scale bedforms (wavelengths up to kilometers and wave heights of tens/hundreds of meters). The paucity of small-scale bedforms detected in deep volcanic settings is likely due to a technological bias related to the exponential decrease in resolution of ship-mounted multibeam bathymetry with increasing water depth. Small-scale bedforms are usually unrecognizable at depths > 400 m (depending on the type and frequency of multibeam system), unless AUV- or ROV-mounted multibeam surveys are performed, as recently observed in the deeper part of active canyon systems (e.g., Paull et al., 2010). On other hand, it is noteworthy that (where data is available) small-scale bedforms are not so common on the upper part of volcanic edifices, especially if compared to non-volcanic settings. This is because volcanic edifices are frequently characterized by steep flanks, with gradients > 20°-30° (Quartau et al., 2010; Romagnoli et al., 2013a), whilst on passive margins, slopes are not steeper than 5º-10º (O'Grady et al., 2000). On such steep gradients, the sediment-laden flows tend to by-pass or erode the seafloor (as evidenced by a network of narrow and steep gullies), hindering the formation of small-scale bedforms (Schlager and Camber, 1986; Micallef and Mountjoy, 2011; Clare et al., 2018). Small-scale bedforms start to develop only when gradients decrease to values less than 15° (Table 1). This threshold can vary slightly between the different areas in relation to the morphological setting and characteristics of the source area (sediment type, flow rheology, and so on). This range of gradients on the upper flanks is often associated to the development of shallow and flat-bottomed channels able to incise the shelf, sometimes cutting back up to the coast (Figs. 6-10). In such cases, a morphological link between these submarine channels and the local drainage network on the island can be envisaged (Figs 8 and 10; Babonneau et al., 2013) Large-scale bedforms occur at all water depths, but they are more commonly observed on the lower part of volcanic flanks. Slope gradients play an important role here also, with the bedforms recognized on slope gradients < 8° (Table 1).

The definition of small- and large-scale bedforms partially reflects the one recently proposed by Symons et al. (2016), where a gap in size between these two kinds of bedforms was observed through statistical analysis of several case-studies. However, by plotting the wavelengths and wave heights of all bedforms observed in this study (Fig. 14), the data suggest that there is a continuity of bedform sizes. This continuity can be explained by interpreting the data that fills the gap shown by Symons et al. (2016) as end-members of small- and large-scale bedforms, respectively. In our opinion, the subdivision between small- and large-scale bedforms is in fact based on process differences:

i) small-scale bedforms mostly occur in confined settings, i.e. within shallow and flat-bottomed channels. However, their size (especially wavelengths and lateral extent) often tend to increase downslope, partially overlapping the smaller sizes of the large-scale bedforms. This is especially true where there are marked changes in slope gradient and/or the confluence of small gullies in a larger and shallower channel;

ii) large-scale bedforms occur in both confined and unconfined settings. Their size is strongly dependent on the setting, distance from source area and characteristics (frequency and energy) of the sediment-laden flows (see section 3.2). However, where part of the bedform train originates in proximal, confined settings, they commonly display smaller sizes which partially overlap with the larger sizes of small-scale bedforms. It is noteworthy that the recognition of bedforms that fill the spatial gap of Symons et al. (2016) is often hard to detect on morpho-bathymetric data acquired with ship-mounted multibeam systems because of the size and range depth (i.e., few thousands of meters) where they develop.

Another interesting finding is that the aspect (H/L) ratio of the recognized bedforms shows a very scattered distribution, ranging from values less than 1:10 to values higher than 1:100 (Fig. 14a). On the other hand, data show that each volcanic edifice is characterized by a specific range of this ratio (especially for large-scale bedforms, Fig. 14b) even if overlapping areas are present among the different case-studies. These differences are less accentuated for small-scale bedforms (Fig. 14c), even if it is noteworthy that in the Tanna case (Fig. 14c), the H/L ratio allows us to distinguish two main bedforms fields within the same area. Here, the smaller bedform field is characterized by larger bedforms with a lower H/L occurring just seaward of a caldera collapse margin. Thus, it appears that underlying structural controls may affect the nature and dimensions of bedform development.

3.2 Processes and factors responsible for the genesis and evolution of the bedforms

In all case-studies, the bedforms generated by sediment-laden flows were found at/or close to relevant sediment sources, i.e. large caldera collapses, subaerial/submarine depressions left by sector collapses, shallow submarine channels directly linked to the subaerial drainage network or able to intercept longshore drift, insular shelf sectors largely indented by landslide scars and/or channelized features. Importantly, the presented examples show that a range of volcanic and non-volcanic processes occurring at different timescales and with different magnitudes can be responsible for their genesis (Table 2).

In addition to sediment sources, regional slope gradient has been identified as a key factor for bedform development, particularly the occurrence of slope breaks. The interaction of flows with breaks in slope favor the development of erosive-depositional bedforms. This is a consequence of breaks in slope forcing flows to pass through a hydraulic jump due to significant flow velocity reduction and thickening (e.g. Postma et al., 2009; Spinewine et al., 2009; Cartigny et al., 2011). By considering the steepness of the submarine volcanic flanks, with values typically > 20° in the upper part and rapidly decreasing to only a few degrees at the base of the edifices, most of these features can be interpreted as upper-regime flows bedforms. Similar evidence is provided by the small-scale bedforms identified at Vanuatu (Fig. 10), Aeolian islands (Figs. 6-9) and La Reunion (Babboneau et al., 2013) which are very similar in size and morphology to upper-flow regime bedforms found in many other subaqueous, non-volcanic settings where repeated seafloor surveys and direct flow monitoring have demonstrated the occurrence of density-stratified turbidity currents that undergo a series of hydraulic jumps (Hughes-Clarke, 2016; Normandeau et al., 2016; Hage et al., 2018; Paull et al., 2018). Similarly, repeated multibeam surveys at Piscità Channel (Stromboli, Fig. 6) evidenced an overall upslope migration of the bedforms through time (Casalbore et al., 2017a), a typical feature associated with upper-flow regime bedforms and a clear indication of active sedimentary dynamics.

The triggering mechanisms for sediment gravity flows which result in bedform formation can be different and in most cases are the result of a cascading effect between volcanic and non-volcanic processes, including:

i) the development of hyperpycnal flows at the mouth of rivers draining volcanic islands. A consequence of sediment-laden river water exceeding the density of seawater (Mulder and Syvitski, 2005), these flows can be triggered by heavy rains or volcanic activity. On most volcanic-arc islands, rivers are characterized by small, steep drainage basins and high magnitude drainage events which favor the development of hyperpycnal flows (Mulder and Syvitski, 2005). Large eruptions can also drastically modify their catchment basins and cause a sudden and large supply of loose easily transported tephras which can greatly increase river sediment loads. This process has, in fact, been monitored during and immediately after the most important eruptions of Mount Pinatubo (Philippines), especially where lahars acted as temporary dams (Newhall and Punongbayan, 1996).

In such cases, once the impounded water is able to overtop the volcanic debris dams, flooding ensued, such as the extremely devastating events in 1991, 1992, and 1994. A quite similar scenario has been recently proposed for the genesis of bedforms at Tanna (Vanuatu, Fig. 10) that can be associated with the impoundment of Lake Isiwi by lava flows and successive outburst floods discharged at the outflow of the Siwi River in 2000 (section 2.5; Clare et al., 2018);

ii) the development of small slope failures at channel heads can be triggered both by seismic/volcanic activity and deformative processes during eruptive events or by cyclic-loading due to storm-waves (depending on the range depth and meteo-marine regime). In such cases, slopes are preconditioned by the progressive infilling and oversteepening of channel heads due to sedimentation driven by subaerial drainage networks or by interception of littoral drift that in active islands can greatly increase during eruptive events, as observed at Stromboli (Fig. 6). Similarly, small retrogressive failures can occur at the edge of the insular shelf or volcaniclastic prograding wedges that commonly overlie the erosive surface of the shelf as recognized in several volcanic edifices (Chiocci et al., 2013; Casalbore et al., 2017; Quartau et al. 2012; 2014), as for instance observed in the NW part of Vulcano (Fig. 9).

The interpretation of large-scale bedforms is often more complex. This is especially true if only bathymetric data are available, because similar features could be also generated by normal faulting along a seafloor-parallel detachment surface, which produces rows of tilted fault blocks in the cases where the failed material does not fully disintegrate downslope (e.g. Micallef et al., 2008; Chiocci et al., 2013; Leat et al., 2010; Pope et al., 2018) or by retrogressive failures (Casalbore et al., 2016). Based on the considerations of Pope et al. (2018) and on the presented case-studies, we propose the following morphological criteria to constrain the origin of bedforms emplaced by slope failures: a) bedforms occur on steep slope (> 15°), b) bedforms are confined within the scar headwall or by two well lateral margins in their upper reaches, c) little to non-change in bedform geometry downslope, especially at or close to break-in-slope of island submarine flanks and, d) a compressional zone is identifiable at the toe of the landslide. However, the main diagnostic criterion is the analysis of their internal geometry by seismic profiles, similarly to what was proposed for large-scale bedforms in non-volcanic settings (Lee et al., 2002; Urgeles et al., 2011; Li et al., 2019). Large-scale bedforms have been shown to exhibit internal seismic reflectors with lateral continuity and upslope migration allowing them to be interpret as upper-flow regime bedforms, as shown by the example shown in Fig. 2. However, it should be noted that the acquisition of seismic profiles able to image the inner geometry of bedforms is often hindered along the flanks of volcanic edifices, because they are commonly characterized by steep slopes and coarse-grained sediments/rocky outcrops.

Based on the associated preconditioning/triggering processes, two main group of large-scale bedforms can be recognized. The first group is more strictly associated with volcano-tectonic processes and they can occur from shallow- to deep-water sectors. These bedforms are mostly observed within or downslope of sector collapse depressions (Stromboli, Fig. 1 ESM; Canary Islands, Wynn et al., 2000) as well as around large caldera collapses (Figs. 2 and 4; Santorini, Croff et al., 2006). In the former case, sector collapses represent a main pathway for the transport of volcaniclastic material from the islands towards deeper sectors, especially when these areas are fed by persistent volcanic activity and thus able to generate frequent and high-energy sedimentary gravity flows, as for instance observed along the Sciara del Fuoco depression at Stromboli (Romagnoli et al., 2009a, Fig. 1 ESM). In the latter case, bedforms are mainly formed by eruption-fed supercritical density flows associated with large explosive eruptions that lead to caldera collapses. A possible relationship between bedforms size and magnitude of explosive eruption can be inferred, as testified by the similarity in size between large-scale bedforms and associated calderas recognized around Santorini, Macauley and Dakatua edifices (Figs 2 and 4, Croff et al., 2006). Such large-scale bedforms appear to be absent on smaller calderas in submarine arc volcanoes, such as Ventotene (Casalbore et al., 2106b) or Vulcano edifices (Fig. 9). However, it is noteworthy that a large amount of volcaniclastic sediments can be delivered to the surrounding marine environment during smaller caldera forming events as well, promoting its successive dismantling through repeated slope failures and associated generation of small-scale bedforms, as for instance observed in the NE part of Vulcano (Fig. 9).

Large-scale bedforms are also lacking on large calderas developed on basaltic volcanoes associated with Mid-Ocean Ridges or intraplate hotspot volcanism, whose formation is often related to syn- or post-eruption collapse following magma withdrawal (e.g., Fornari et al. 1984).

The second group of large-scale bedforms only develop in the deeper part of the submarine drainage networks affecting insular volcanoes and they are commonly unrelated to significant volcano-tectonic events. Here, the bedforms are associated with an abrupt break-in-slope from gradients of 20°-30° to gradients of less than 3°-5°, often matching a change from confined to unconfined settings, as observed around Madeira Archipelago (Figs. 11, 12, 13, 2 ESM and 3 ESM), Panarea and SW Vulcano (Fig. 1 ESM). This change could promote the formation of hydraulic jumps in the sediment-laden flows and thus the formation of upper-flow regime bedforms (Symons et al., 2016). The sediment-laden flows can be triggered by several processes, including i) large hyperpycnal flows generated at subaerial rivers, especially on wide oceanic islands where well-developed subaerial drainage can develop (especially if compared to steep and smaller volcanic arc ones), such as at Madeira (Quartau et al., 2018) or La Reunion islands (Sisavath et al., 2011; Mazuel et al., 2016), ii) retrogressive slope failures occurring along the sidewalls and headwall of submarine channels. Most of these channels indent the insular shelf edge, where a significant amount of volcaniclastic deposits can be stored during highstand and transgressive system tracts and successively remobilized downslope (especially during lowstands periods), as observed at the Aeolian, Madeira and Azores Archipelago (Casalbore et al., 2017; Quartau et al., 2012; 2014; 2015).

Conclusions

The comparison of bedforms fields along the submarine flanks of several insular volcanoes has provided insights into their size distribution and controlling factors in a range of different geodynamic setting, morpho-structural evolution, volcanic and oceanographic regimes. Our data indicate that a previously identified spatial gap in wavelength/wave height ratio may be an artifact of data resolution, and is not a true gap in the natural world. Therefore, we recommend the analysis of ancillary data (side scan sonar images and seismic profiles) coupled with a re-processing or new collection of high-resolution multibeam bathymetry along the middle and lower part of volcanic flanks to verify the possible occurrence of further examples of bedforms that fill this spatial gap. We do identify, however, a general distinction between small- (wavelengths of 10s/100s of meters and wave heights of some meters) and large-scale (wavelengths of 100s/1000s of meters and wave height of 10s/100s of meters) bedforms. In both cases, the bedforms are associated with major sediment sources and slope gradients play a key role in their development; with a maximum threshold of 15° and 8° for small and large bedforms, respectively. Specifically, small-scale bedforms are mainly found in confined settings, i.e. the thalweg of shallow and flat-bottomed channels that carve the shelf surrounding volcanic islands. These small-scale bedforms are interpreted as the result of cyclic erosional-depositional processes associated with density flows that fluctuate between super- and subcritical modes, similarly to the bedforms observed in active channels and prodeltas elsewhere. The flows are related to a combination of volcanic and non-volcanic processes, among which sudden flood discharge or slope failures are the most common. For small-scale bedforms, we recommend performing repeated multibeam surveys to monitor their morphological evolution, as it can provide identification of their development and associated triggering mechanisms.

The interpretation of large-scale bedforms is more challenging, as they can be related to seafloor displacement induced by slope failures or cyclic erosional-depositional processes associated with density currents. Even if some morphological criteria are proposed to distinguish between these two types of bedforms (slope gradients, degree of confinement within landslide scars or downslope occurrence of compressional features, along-slope change in bedforms geometry), we recommend the use of seismic profiling and core data to better constrain their internal geometry and prevent erroneous interpretations. Large-scale bedforms generated by density currents occur both in confined and unconfined setting and they are often associated with main volcano-tectonic events, such as large flank or caldera collapses. Alternatively, large-scale bedforms can be observed on lower volcanic flanks at or close to marked breaks-in-slope (from 20°-30° to values of few degrees), often matching a change from confined to unconfined settings. Such breaks-in-slope favor the formation of hydraulic jumps in large supercritical sediment-laden flows sourced from large depressions left by flank collapses, landslide scars affecting the insular shelf edge or reworking of caldera infilling. Data also show that the aspect (H/L) ratio of the bedforms (a parameter commonly used for their characterization) is generally scattered, but its range varies among the different edifices and/or in correspondence of abrupt morphological changes, suggesting that underlying morpho-structural controls may control the nature and dimensions of the bedforms.

In summary, the results of this study show that erosional-depositional bedforms are a common geomorphic feature observed in marine volcaniclastic settings and their morphometric characterization provides insights on the associated density flows and more generally on the transfer of sediments from the tip to the base of the insular volcanoes. These inferences can be useful also to assess the geohazard associated with large turbidite or eruption-fed pyroclastic flows generated at volcanic islands and offshore areas, that can destructively impact offshore infrastructure.

Acknowledgements

We would like to thank the New Zealand National Institute of Water and Atmospheric Research (NIWA) for providing access to the Macauley Volcano dataset. Dr. Gary Hoffman, Dr. Eli Silver and Dr. Phil Leat are thanked for making their bathymetry datasets of the South Sandwich Islands and New Britain publically available. E. Pope was supported by a Leverhulme Early Career Fellowship (ECF-2018-267). M. Clare was supported by NERC CLASS project (grant number NE/R015953/1). DPC-INGV and MaGIC (Marine Geohazards Along the Italian Coast) projects are gratefully acknowledged to provide funding for data acquisition around Aeolian Islands as well as ship-time provided by National Research Council of Italy aboard R/V Urania, Thetis and Minerva 1. Officials and crews of these vessels are gratefully acknowledged along with the researchers and students taking part in the surveys.

References

Babonneau, N., Delacourt, C., Cancouët, R., Sisavath, E., Bachèlery, P., Mazuel, A., Jorry, S.J.,

Deschamps, A., Ammann, J., Villeneuve, N. (2013) Direct sediment transfer from land to deep-sea: insights into shallow multibeam bathymetry at La Réunion Island. *Mar Geol*, **346,** 47–57

Baioni, D. (2011) Human activity and damaging landslides and floods on Madeira Island. *Nat. Hazards Earth Syst. Sci*. **11,** 3035-3046**.**

Barker, S.J., Wilson, C.J.N., Baker, J.A., Millet, M.-A., Rotella, M.D., Wright, I.C., Wysoczanski, R.J. (2012). Geochemistry and petrogenesis of silicic magmas in the intra-oceanic Kermadec arc. J Petrol, **54**, 351-391.

Bell, K.L.C. (2011). On the origin of submarine sediment features in the southern Aegean Sea. Ph.D. thesis. University of Rhode Island

Blake, D.H., Bleeker, P. (1970) Volcanoes of the Cape Hoskins area, New Britain, territory of Papua and New Guinea. *Bulletin Volcanologique* **34**, 385-405.

Bosman, A., Casalbore, D., Romagnoli, C., & Chiocci, F. L. (2014). Formation of an 'a'ā lava delta: insights from time-lapse multibeam bathymetry and direct observations during the Stromboli 2007 eruption. *Bull Volcanol*, **76**(7), 838.

Boudon, G., Le Friant, A., Komorowski, J.-C., Deplus, C., Semet, M. (2007) Volcano flank instability in the Lesser Antilles Arc: diversity of scale, processes, and temporal recurrence. *J. Geophys. Res.* **112**, B08205. doi:10.1029/2006JB004674.

Carey, S. (2000) Volcaniclastic sedimentation around island arcs. In: *Encyclopedia of volcanoes* (Ed. H. Sigurdsson). Academic Press, San Diego, pp. 627–642.

Carter, L., Gavey, R., Talling, P. J., Liu, J. T. (2014). Insights into submarine geohazards frombreaks in subsea telecommunication cables. *Oceanography* **27**, 58–67. doi: 10.5670/oceanog.2014.40

Cartigny, M.J.B., Postma, G., van den Berg, J.H., Mastbergen, D.R. (2011) A comparative study of sediment waves and cyclic steps based on geometries, internal structures and numerical modeling. *Mar Geol* **280**, 40-56.

Cas, RAF, Simmons, JM (2018) Why Deep-Water Eruptions Are So Different From Subaerial Eruptions. *Front. Earth Sci.* 6, 198. doi: 10.3389/feart.2018.00198

Casalbore, D. (2018) Volcanic islands and seamounts. In: *Submarine Geomorphology*. Springer, Cham, 333-347.

Casalbore, D., Bosman, A., Martorelli, E., Sposato, F.L., Chiocci, F.L. (2016b) Mass wasting features on the submarine flanks of Ventotene volcanic edifice (Tyrrhenian Sea, Italy). In: *Submarine Mass Movements and Their Consequences* (Eds Krastel, et al.), **37**, 285–293.

Casalbore, D., Bosman, A., Romagnoli, C., Chiocci, F. L. (2017a) Small-scale bedforms generated by gravity flows in the Aeolian Islands. In *Atlas of Bedforms in the Western Mediterranean*. Springer, Cham pp. 287-292

Casalbore, D., Romagnoli, C., Bosman, A., Chiocci, F.L. (2014). Large-scale seafloor waveforms on the flanks of insular volcanoes (Aeolian Archipelago, Italy), with inferences about their origin. *Mar. Geol.* **355**, 318–329.doi: 10.1016/j.margeo.2014.06.007

Casalbore, D., Romagnoli, C., Bosman, A., Anzidei, M., Chiocci, F. L. (2018). Coastal hazard due to submarine canyons in active insular volcanoes: examples from Lipari Island (southern Tyrrhenian Sea). *J Coast Conserv*, **22**(5), 989-999.

Casalbore, D., Romagnoli, C., Pimentel, A., Quartau, R., Casas, D., Ercilla, G., Hipolito, A., Sposato, A., Chiocci, F.L. (2015) Volcanic, tectonic and mass-wasting processes offshoreTerceira island (Azores) revealed by high-resolution seafloor mapping. *Bull. Volcanol*., **77** (3)

Casalbore, D, Bosman, A, Romagnoli, C, Chiocci, FL (2013) Small-scale crescent-shaped bedforms in submarine volcanic setting: examples from Stromboli and Salina island (Italy). *GeoActa*, **12**, 37-45.

Casalbore, D., Bosman, A., Romagnoli, C., Di Filippo, M., Chiocci, F. L. (2016). Morphology of Lipari offshore (Southern Tyrrhenian Sea). *Journal of Maps*, **12(1),** 77-86.

Casalbore, D, Falese, F, Martorelli, E, Romagnoli, C, Chiocci, FL (2017b) Submarine depositional terraces in the Tyrrhenian sea as a proxy for paleo-sea level reconstruction: problems and perspective. *Quat Int* **439**,169–180

Chadwick Jr., W.W., Cashman, K.V., Embley, R.W., Matsumoto, H., Dziak, R.P., de Ronde, C.E.J., Lau, T.K., Deardorff, N.D., Merle, S.G. (2008) Direct video and hydrophone observations of submarine explosive eruptions at NW Rota-1 volcano, Mariana arc. *Journal of Geophysical Research*: *Solid Earth* 113.

Chen, J. K., Taylor, F. W., Edwards, R. L., Cheng, H., Burr, G.S. (1995). Recent emerged reef terraces of the Yenkahe resurgent block, Tanna, Vanuatu: implications for volcanic, landslide and tsunami hazards. *The Journal of Geology*, **103(5)**, 577-590.

Chiocci, F.L., Casalbore, D. (2017). Unexpected fast rate of morphological evolution of geologically-active continental margins during Quaternary: Examples from selected areas in the Italian seas. *Marine and Petroleum Geology*, **82**, 154-162.

Chiocci, FL, Romagnoli, C, Tommasi, P, Bosman, A (2008) Stromboli 2002 tsunamigenic submarine slide: characteristics and possible failure mechanisms. *J Geophys Res,* **113**, B10102.

Chiocci FL, Romagnoli C, CasalboreD et al (2013) Bathy-morphological setting of Terceira island (Azores) after the FAIVI cruise. *J Maps* **9**, 590–595.

Clare, M. A., Clarke, J. H., Talling, P. J., Cartigny, M. J. B., and Pratomo, D. G. (2016). Preconditioning and triggering of offshore slope failures and turbidity currents revealed by most detailed monitoring yet at a fjordhead delta. *Earth Planetary Sci. Lett.* **450**, 208–220. doi: 10.1016/j.epsl.2016.06.021

Clare, MA, Le Bas, T, Price, DM, Hunt, JE, Sear, D, Cartigny, MJB, Vellinga, A, Symons W, Firth C, Cronin, S (2018) Complex and Cascading Triggering of Submarine Landslides and Turbidity Currents at mVolcanic Islands Revealed From mIntegration of High-Resolution Onshore and Offshore Surveys. *Front. Earth Sci.,* **6**,223. mdoi: 10.3389/feart.2018.00223

Coombs, M.L., White, S.M., Scholl, D.W. (2007) Massive edifice failure at Aleutian Arc volcanoes. *Earth Planet. Sci. Lett.* doi:10.1016/j.epsl.2007.01.030.

Firth, C. W., Cronin, S. J., Turner, S. P., Handley, H. K., Gaildry, C., Smith, I. (2015). Dynamics and pre-eruptive conditions of catastrophic, ignimbrite-producing eruptions from the Yenkahe Caldera, Vanuatu. *J Volcanol Geoth Res*, **308**, 39-60.

Fornari, DJ, Ryan, WBF, Fox, PJ (1984) The evolution of craters and calderas on young seamounts: insights from sea MARC1 and SEABEAM sonar surveys of a small seamount group near the axis of the East Pacific Rise at 108N. *J Geophys Res* **89**,11069–11083

Gardner, J.V. (2010) The West Mariana Ridge, western Pacific Ocean: geomorphology and processes from new multibeam data. *Geol. Soc. Am. Bull.*, **122**, 1378–1388.

Geldmacher, J., Hoernle, K., van den Bogaard, P., Zankl, G., Garbe-Schonberg, D. (2001) Earlier history of the >= 70-Ma-old Canary hotspot based on the temporal and geochemical evolution of the Selvagen Archipelago and neighboring seamounts in the eastern North Atlantic. *J. Volcanol. Geotherm. Res.* **111**, 55-87.

Geldmacher, J., van den Bogaard, P., Hoernle, K., Schmincke, H.-U. (2000) The 40Ar/39Ar age dating of the Madeira Archipelago and hotspot track (eastern North Atlantic). *Geochem. Geophys. Geosyst.* **1**, 1-26.

Hage, S., Cartigny, M. J., Clare, M. A., Sumner, E. J., Vendettuoli, D., Hughes Clarke, J. E., et al. (2018). How to recognize crescentic bedforms formed by supercritical turbidity currents in the geologic record: insights from active submarine channels. *Geology* **46**, 563–566. doi: 10.1130/G40095.1.

Hampton, M.A., Lee, H.J., Locat, J. (1996) Submarine landslides. *Reviews of Geophysics* **34**, 33-59.

Hoffmann, G., Silver, E., Day, S., Driscoll, N., Orange, D. (2011) Deformation versus deposition of sediment waves in the Bismarck Sea, Papua New Guinea. Mass-transport deposits in deepwater settings. *SEPM Spec Publl* **96**, 455-474.

Hoffmann, G., Silver, E., Day, S., Morgan, E., Driscoll, N., Orange, D. (2008) Sediment waves in the Bismarck volcanic arc, Papua New Guinea. *Geological Society of America Special Papers* **436**, 91-126.

Hughes Clarke, J. E. (2016). First wide-angle view of channelized turbidity currents links migrating cyclic steps to flow characteristics. *Nat Commun.* **7**,11896. doi: 10.1038/ncomms11896.

Larter, R.D., Vanneste, L.E., Morris, P., Smythe, D.K. (2003) Structure and tectonic evolution of the South Sandwich arc. *Geological Society, London, Special Publications* **219**, 255-284.

Lee, H.J., Syvitski, J.P.M., Parker, G., Orange, D., Locat, J., Hutton, E.W.H., Imran, J. (2002) Distinguishing sediment waves from slope failure deposits: field examples, including the "Humboldt Slide" and modeling results. *Mar Geol* **192**, 79–104.

Leat, P.T., Smellie, J.L., Millar, I.L., Larter, R.D. (2003) Magmatism in the South Sandwich arc. *Geological Society, London, Special Publications* **219**, 285-313.

Leat, P.T., Tate, A.J., Tappin, D.R., Day, S.J., Owen, M.J. (2010) Growth and mass wasting of volcanic centers in the northern South Sandwich arc, South Atlantic, revealed by new multibeam mapping. *Mar Geol*, **275**, 110-126.

Li, J., Li, W., Alves, T. M., Rebesco, M., Zhan, W., Sun, J., Mitchell, N., Wu, S. (2019). Different origins of seafloor undulations in a submarine canyon system, northern South China Sea, based on their seismic character and relative location. *Mar Geol*, **413**, 99-111.

Lloyd, E.F., Nathan, S., Smith, I.E.M., Stewart, R.B. (1996) Volcanic history of Macauley Island, Kermadec Ridge, New Zealand. *Journal of Geology and Geophysics* **39**, 295-308.

Lowder, G.G., Carmichael, I.S.E. (1970) The volcanoes and caldera of Talasea, New Britain: geology and petrology. *Geological Society of America Bulletin* **81**, 17-38.

Lucchi, F., Keller, J., & Tranne, C. A. (2013). Regional stratigraphic correlations across the Aeolian archipelago (southern Italy). In: *The Aeolian Islands Volcanoes* (Eds Lucchi, F., Peccerillo, A., Keller, J., Tranne, C.A., Rossi, P.L.). Geological Society, London. Memoirs, 37, pp. 56–81.

Mazuel, A., Sisavath, E., Babonneau, N., Jorry, S.J., Bachèlery, P., Delacourt, C. (2016) Turbidity current activity along the flanks of a volcanic edifice: the mafate volcaniclastic complex, La Réunion Island, Indian Ocean. *Sediment. Geol.* **335**, 34–50.

McGuire, W. J. (2006). Lateral collapse and tsunamigenic potential of marine volcanoes. *Geological Society, London, Special Publications*, **269**(1), 121-140.

Menard, H.W. (1956) Archipelagic aprons. *AAPG Bulletin* **40**, 2195–2210.

Merle, O., Brothelande, E., Lénat, J. F., Bachèlery, P., Garaébiti, E. (2013). A structural outline of the Yenkahe volcanic resurgent dome (Tanna Island, Vanuatu Arc, South Pacific). *J Volcanol Geoth Res*, **268**, 64-72.

Micallef, A., Mountjoy, J. J. (2011). A topographic signature of a hydrodynamic origin for submarine gullies. *Geology*, **39(2),** 115-118

Micallef, A., Berndt, C., Masson, D.G., Stow, D.A.V. (2008) Scale invariant charac-teristics of the Storegga Slide and implications for large-scale submarine mass movements. *Mar. Geol.* **247**, 46–60.

Mitchell, N.C., Masson, D.G., Watts, A.B., Gee, M.J.R., Urgeles, R. (2002) The morphology of the submarine flanks of volcanic ocean islands. A comparative study of the Canary and Hawaiian hotspot islands. J Volcanol Geoth Res, **115**, 83–107.

Mitchell NC, Beir C, Rosin PL, Quartau R, Tempera F (2008) Lava penetrating water: submarine lava flows around the coasts of Pico Island, Azores. *Geochem Geophys Geosyst* , **9**, Q03024. doi:10. 1029/2007GC001725

Mulder, T, Syvitski, JPM (1995) Turbidity currents generated at mouths of rivers during exceptional discharges to the world oceans. *J Geol* **103**, 285–299.

Nairn, I.A., Scott, B.J. and Giggenbach, W.F. (1988). Yasur volcano investigations, Vanuatu, September 1988. *New Zealand Geological Survey Report*, G134, 74

Neall, V.E., Wallace, R.C., Torrence, R. (2008) The volcanic environment for 40,000 years of human occupation on the Willaumez Isthmus, West New Britain, Papua New Guinea. *J Volcanol Geoth Res* **176**, 330-343.

Newhall, C.G., Punongbayan, R.S. (1996) Fire and mud: Eruptions and lahars of Mount Pinatubo: Seattle, University of Washington Press, 1126 p.

Normandeau, A., Lajeunesse, P., Poiré, A. G., and Francus, P. (2016). Morphological expression of bedforms formed by supercritical sediment density flows on four fjord-lake deltas of the south-eastern Canadian Shield (Eastern Canada). *Sedimentology* **63**, 2106–2129. doi: 10.1111/sed.12298.

O'Grady, D.B., Syvitski, J.P.M, Pratson, L.F., Sarg, J.F. (2000) Categorizing the morphologic variability of siliciclastic passive continental margins. *Geology*, **28**, 207-210.

Omira, R., Quartau, R., Ramalho, R., Baptista, M.A., Mitchell, N.C. (2016) The tsunami effects of a large-scale flank collapse on a semi-enclosed basin: the Pico-S. Jorge channel in the Azores archipelago**.** In: *Plate Boundaries and Natural Hazards* (Eds. Duarte, J.C., Schellart, W.P.). John Wiley & Sons, Inc, New Jersey, pp. 271–287.

Paull, C.K., Ussler III,W., Caress, D.W., Lundsten, E., Barry, J., Covault, J.A., Maier, K.L., Xu, J.P., Augenstein, S. (2010) Origins of large crescent-shaped bedformswithin the axial channel of Monterey Canyon. *Geosphere* **6**, 755–774

Pearce, J.A., Baker, P.E., Harvey, P.K., Luff, I.W. (1995) Geochemical evidence for subduction fluxes, mantle melting and fractional crystallization beneath the South Sandwich island arc. *Journal of Petrology* **36**, 1073-1109.

Pope, E.L., Jutzeler, M., Cartigny, M.J.B., Shreeve, J., Talling, P.J., Wright, I.C., Wysoczanski, R.J. (2018) Origin of spectacular fields of submarine sediment waves around volcanic islands. *Earth and Planetary Science Letters*, **493**, 12-24.

Pope, E. L., Talling, P. J., Carter, L., Clare, M. A., and Hunt, J. E. (2017). Damaging sediment density flows triggered by tropical cyclones. *Earth Planet. Sci. Lett.*, **458**, 161–169. doi: 10.1016/j.epsl.2016.10.046.

Postma, G., Cartigny, M., Kleverlaan, K. (2009) Structureless, coarse-tail graded Bouma Ta formed by internal hydraulic jump of the turbidity current? *Sedimentary Geology* **219 (1–4)**, 1–6.

Quartau, R., Ramalho, R.S., Madeira, J., Santos, R., Rodrigues, A., Roque, C., Carrara, G., da Silveira, A.B. (2018) Gravitational, erosional and depositional processes on volcanic ocean islands: Insights from the submarine morphology of Madeira Archipelago. *Earth and Planetary Science Letters*, **482**, 288-299.

Quartau R, Hipólito A, Romagnoli C, Casalbore D, Madeira J, Tempera F, Roque C, Chiocci FL (2014) The morphology of insular shelves as a key for understanding the geological evolution of volcanic islands: insights from Terceira Island (Azores). *Geochem Geophys Geosy* **15**,1801–1826.

Quartau, R, Trenhaile, AS, Mitchell, NC, Tempera, F (2010) Development of volcanic insular shelves: Insights from observations and modelling of Faial Island in the Azores Archipelago. *Mar Geol* **275**, 66–83

Quartau, R, Tempera, F, Mitchell, NC, Pinheiro, LM, Duarte, H, Brito, PO, Bates, R, Monteiro, JH (2012) Morphology of the Faial Island shelf (Azores): the interplay between volcanic, erosional, depositional, tectonic and mass-wasting processes. *Geochem Geophys Geosy* **13**, Q04012

Quartau, R., Madeira, J., Mitchell, N. C., Tempera, F., Silva, P. F., & Brandão, F. (2015). The insular shelves of the Faial-Pico Ridge (Azores archipelago): A morphological record of its evolution. *Geochemistry, Geophysics, Geosystems*, **16**(5), 1401-1420.

Ramalho, R. S., Quartau, R., Trenhaile, A. S., Mitchell, N. C., Woodroffe, C. D., Avila, S. P. (2013). Coastal evolution on volcanic oceanic islands: A complex interplay between volcanism, erosion, sedimentation, sea-level change and biogenic production. *Earth-Science Reviews*, **127**, 140-170.

Ramalho, R.S., Brum da Silveira, A., Fonseca, P., Madeira, J., Cosca, M., Cachão, M., Fonseca, M., Prada, S. (2015) The emergence of volcanic oceanic islands on a slow-moving plate: the example of Madeira Island, NE Atlantic. *Geochem. Geophys. Geosyst.* **16,** 522–537.

Romagnoli, C., Casalbore, D., Ricchi, A., Lucchi, F., Quartau, R., Bosman, A., Tranne, C.A., Chiocci, F. L. (2018). Morpho-bathymetric and seismo-stratigraphic analysis of the insular shelf of

Salina (Aeolian archipelago) to unveil its Late-Quaternary geological evolution. *Mar Geol*, **395**, 133-151.

Romagnoli, C, Casalbore, D, Bortoluzzi, G, Bosman, A, Chiocci, FL, D'Oriano F, Gamberi, F, Ligi, M, Marani, M (2013a) Bathymorphological setting of the Aeolian islands. In: *The Aeolian Islands Volcanoes* (Eds Lucchi F, Peccerillo A, Keller J, Tranne CA, Rossi PL), vol 37. Geological Society, London, Memoirs, pp 27–36.

Romagnoli, C, Casalbore, D, Bosman, A, Braga, R, Chiocci, FL (2013b) Submarine structure of Vulcano volcano (Aeolian islands) revealed by high-resolution bathymetry and seismo-acoustic data. *Mar Geol* **338**, 30–45

Romagnoli, C., Casalbore, D., Chiocci, F.L. (2012) La Fossa Caldera breaching and submarine erosion (Vulcano island, Italy). *Mar. Geol* **303–306**, 87–98.

Romagnoli, C., Kokelaar, P., Casalbore, D., Chiocci, F.L. (2009a) Lateral collapses and active sedimentary processes on the northwestern flank of Stromboli volcano. *Mar Geol* **265**, 101–119.

Romagnoli, C., Mancini, F., & Brunelli, R. (2006). Historical shoreline changes at an active island volcano: Stromboli, Italy. *Journal of Coastal Research*, 739-749.

Rosi, M., Bertagnini, A., Landi, P. (2000) Onset of persistent activity at Stromboli volcano (Italy). *Bull Volcanol* **62**, 294–300.

Santos, R., Quartau, R., da Silveira, A. B., Ramalho, R., & Rodrigues, A. (2019). Gravitational, erosional, sedimentary and volcanic processes on the submarine environment of Selvagens Islands (Madeira Archipelago, Portugal). *Mar Geol.*, **415**, 105945.

Schlager, W. and Camber, O. (1986). Submarine slope angles, drowning unconformities, and self-erosion of limestone escarpments. *Geology*, **14(9)**, 762-765.

Schmidt, R., Schmincke, H.-U. (2002) From seamount to oceanic island, Porto Santo, central East-Atlantic. *Int. J. Earth Sci.* (Geol. Rundsch) **91**, 594-614.

Schwarz, S., Klügel, A., van den Bogaard, P., Geldmacher, J. (2005) Internal structure and evolution of a volcanic rift system in the eastern North Atlantic: the Desertas rift zone, Madeira archipelago. J. *Volcanol. Geotherm. Res*. **141**, 123-155

Shane, P., Wright, I.C. (2011) Late Quaternary tephra layers around Raoul and Macauley Islands, Kermadec Arc: implications for volcanic sources, explosive volcanism and tephrochronology. *J Quaternary Sci* **26**, 422-432.

Silver, E., Day, S., Ward, S., Hoffmann, G., Llanes, P., Driscoll, N., Appelgate, B., Saunders, S. (2009) Volcano collapse and tsunami generation in the Bismarck volcanic arc, Papua New Guinea. *Journal of Volcanology and Geothermal Research*, **186**, 210-222.

Silver, E.A., Abbott, L.D., Kirchoff-Stein, K.S., Reed, D.L., Bernstein-Taylor, B., Hilyard, D. (1991) Collision propagation in Papua New Guinea and the Solomon Sea. *Tectonics* **10**, 863-874.

Sisavath, E., Babonneau, N., Saint-ange, F., Bachèlery, P., Jorry, S.J., Deplus, C., De Voogd, B., Savoye, B. (2011) Morphology and sedimentary architecture of a modern volcaniclastic turbidite system: the Cilaos fan, offshore La Réunion Island. *Mar Geol*, **288**, 1–17

Smith, I.E.M., Stewart, R.B., Price, R.C. (2003) The petrology of a large intra-oceanic silicic eruption: the Sandy Bay Tephra, Kermadec Arc, Southwest Pacific. *J Volcanol Geoth Res* **124**, 173-194.

Spinewine, B., Sequeiros, O.E., Garcia, M.H., Beaubouef, R.T., Sun, T., Savoye, B. (2009) Experiments on wedge-shaped deep-sea sedimentary deposits in minibasins and/or on channel levees emplaced by turbidity currents. Part II. Morphodynamic evolution of the wedge and of the associated bedforms. *Journal of Sedimentary Research* **79 (8)**, 608.

Symons, W.O., Sumner, E.J., Talling, P.J., Cartigny, M.J.B., Clare, M.A. (2016) Large-scale sediment waves and scours on the modern seafloor and their implications for the prevalence of supercritical flows. *Mar. Geol.* **371**, 130–148.

Tappin, D.R., Watts, P., Grilli, S.T. (2008). The Papua New Guinea tsunami of 17 July 1998: anatomy of a catastrophic event. *Natural Hazards and Earth System Science*, **8**(2), 243-266.

Wright, I.C., Worthington, T.J., Gamble, J.A. (2006) New multibeam mapping and geochemistry of the 30–35 S sector, and overview, of southern Kermadec arc volcanism. *J Volcanol Geoth Res*, **149**, 263-296.

Wynn, R.B., Masson, D.G., Stow, D.A.V., Weaver, P.P.E. (2000) Turbidity current sediment waves on the submarine slopes of the western Canary Islands. *Mar Geol*, **163**, 185–198.

Wynn, R.B., Piper, D.J.W., Gee, M.J.R. (2002) Generation and migration of coarse-grained sediment waves in turbidity current channels and channel–lobe transition zones. *Mar Geol* **192**, 59-78.

Additional References (ESM)

Bosman, A., Casalbore, D., Anzidei, M., Muccini, F., Carmisciano, C., Chiocci, F.L. (2015) *Ann. Geophys.*, **58**, S0218. doi:10.4401/ag-6746.

Casalbore, D., Romagnoli, C., Chiocci, F., Frezza, V. (2010) Morphosedimentary characteristics of the volcanic apron around Stromboli volcano. *Mar Geol* **269** (3–4), 132–148.

Chiocci, F.L., Romagnoli, C. (2004) Terrazzi deposizionali sommersi nelle Isole Eolie. *Mem. Descr. Carta Geol. Ital.*, **58**, 81–114.

Romagnoli, C., Casalbore, D., Chiocci, F.L., Bosman, A. (2009b) Offshore evidence of largescale lateral collapse on the eastern flank of Stromboli, Italy, due to structurally controlled, bi-lateral flank instability. *Mar Geol* **262**, 1–13.

Rothwell, R. G., Hoogakker, B., Thomson, J., Croudace, I. W., & Frenz, M. (2006). Turbidite emplacement on the southern Balearic Abyssal Plain (western Mediterranean Sea) during Marine Isotope Stages 1–3: an application of ITRAX XRF scanning of sediment cores to lithostratigraphic analysis. *Geological Society, London, Special Publications*, **267**(1), 79-98.

Tate, A.J., Leat, P.T. (2007) RRS James Clark Ross JR168 cruise report: swath bathymetry South Sandwich Islands, British Antarctic Survey Reprot ES6/1/2007/1, https://www.bodc.ac.uk/data/information_and_inventories/cruise_inventory/report/9079.

Figure Captions

Figure 1 Location of the study-areas presented in this paper. Bathymetry was downloaded from GEBCO and EMODNET website

Figure 2. a) Map of bedforms surrounding Macauley Volcano. Bedform fields and associated bathymetric profilers (A' – F') included in Table 1 are indicated. UFR = Upper-Flow Regime. MM = Mass Movement. b) Un-interpreted seismic data perpendicular to the expected direction of flow of an eruption-fed sediment density flow. c) Trace interpretation of seismic reflectors within the bedforms. The green line represents an interpreted unconformity within the bedforms. d) Bathymetric profiles along the centre of the bedform fields described in Table 1.

Figure 3. a) Map of bedforms surrounding Zavodovski Volcano. Bedform fields included in Table 1 are indicated. UFR = Upper-Flow Regime. MM = Mass Movements. b – d) Bathymetric profiles and slope gradients along the profiles of the bedform fields identified in a).

Figure 4. a) Map of bedforms surrounding Dakataua Caldera. Bedform fields included in Table 1 are indicated. UFR = Upper-Flow Regime. b – c) Bathymetric profiles and slope gradients along the profiles of the bedform fields identified in a).

Figure 5. a) Map of bedforms on the seafloor of Kimbe Bay. Bedform field KB is included in Table 1. UFR = Upper-Flow Regime. b) Bathymetric profile and slope gradient along profile A – A' in a).

Figure 6 a) Shaded relief map of the Piscità channel, where the bedforms field Str4 (location in Fig. 1 and 1ESM) is recognizable; below, bathymetric sections (dark line) and slope gradients (grey-line) extracted from 2013 DEM are showed. b) Residual map between 2002 and 2003 bathymetries collected before and after the Stromboli 2002 eruption and tsunamigenic landslide, evidencing a main migration of bedforms on the eastern side of the channel. c) Residual map between 2013 and 2015 bathymetries collected before and after the 2014 Stromboli eruption, showing the migration of the bedforms mainly on the eastern side of the channel.

Figure 7 Shaded relief map of the Northern Salina channel, where the bedforms field Sal1 (location in Fig. 1 and 1 ESM) is recognizable; on the right, bathymetric sections (dark line) and slope gradients (grey-line) extracted from the DEM are showed

Figure 8 Shaded relief map of the eastern flank of Salina, where the bedforms field Sal2 (location in Fig. 1 and 1 ESM) is recognizable; on the right, bathymetric sections (dark line) and slope gradients (grey-line) extracted from the DEM are showed

Figure 9 Shaded relief map of the northern flank of Vulcano, where the bedforms fields Vul2 and Vul3 (location in Fig. 1 and 1ESM) are recognizable in the NW and NE flank, respectively; on the right and below, bathymetric sections (dark line) and slope gradients (grey-line) extracted from the DEM are showed.

Figure 10 Shaded relief map to illustrate bedform fields offshore Tanna Island, Vanuatu including (A) overview and detailed close-up views (B-D) showing small-scale bedforms. Profiles (F-N) illustrate the variability in scale of bedforms from proximal to distal, as well as in response to topographic changes seaward of the interpreted former caldera collapse (E)

Figure 11 Shaded relief map of the eastern side of Desertas and southern side of Porto Santo where the bedforms MA1 and MA2 were identified. DS1 to DS4 are bathymetric profiles and slope gradients along the profiles of the bedform fields identified in the upper image. Location in Fig. 1 and Fig.2 ESM

Figure 12 Shaded relief map of the northern side of Porto Santo where the bedforms MA3 were identified. PS1 to PS5 are bathymetric profiles and slope gradients along the profiles of the bedform fields identified in the upper image. Location of PS1 is shown in Fig. 11

Figure 13 Shaded relief map of Selvagens where the bedforms SEL 1-4 were identified. SV1 to SV5 are bathymetric profiles and slope gradients along the profiles of the bedform fields identified in the upper image.

Figure 14 (a) Plot of wave height versus wavelength for all the recognized bedforms. Boundaries of H/L ratio for the large-scale (b) and small-scale (c) bedform fields recognized in the different case-studies. The dashed lines are referred to 1:10, 1:25, 1:50, 1:100 H/L values.

Figure 1 ESM Shaded relief map of the five insular volcanoes making up the central and eastern sectors of the Aeolian Archipelago, with the location of the large-scale (from Casalbore et al., 2014) and small-scale bedform fields described in this study (Figs. 6-9). The main submarine morphological features useful to understand the genesis of the bedforms are also drawn. The inset shows the regional setting of the area, where triangles represent submarine seamounts also belonging to the Aeolian Arc.

Figure 2 ESM - Shaded relief map of subaerial and submarine part of Madeira, Porto Santo and Desertas Islands with bedform fields identified MA1 to MA5.

Figure 3 ESM - Shaded relief map of the northern side of Madeira where the bedforms MA4 and MA5 were identified. MAD1 to MAD4 are bathymetric profiles and slope gradients along the profiles of the bedform fields identified in the upper image.

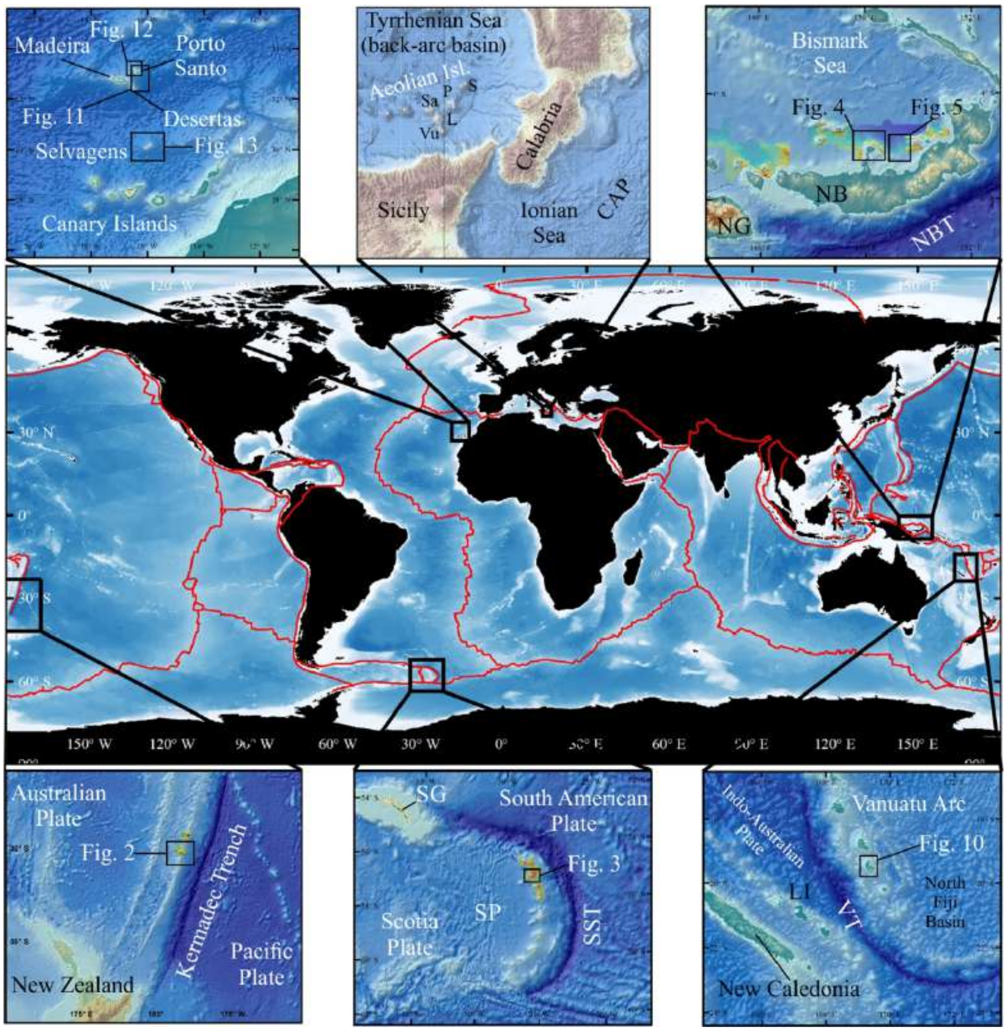

Figure 1 Location of the study-areas presented in this paper. Bathymetry was downloaded from GEBCO and EMODNET website

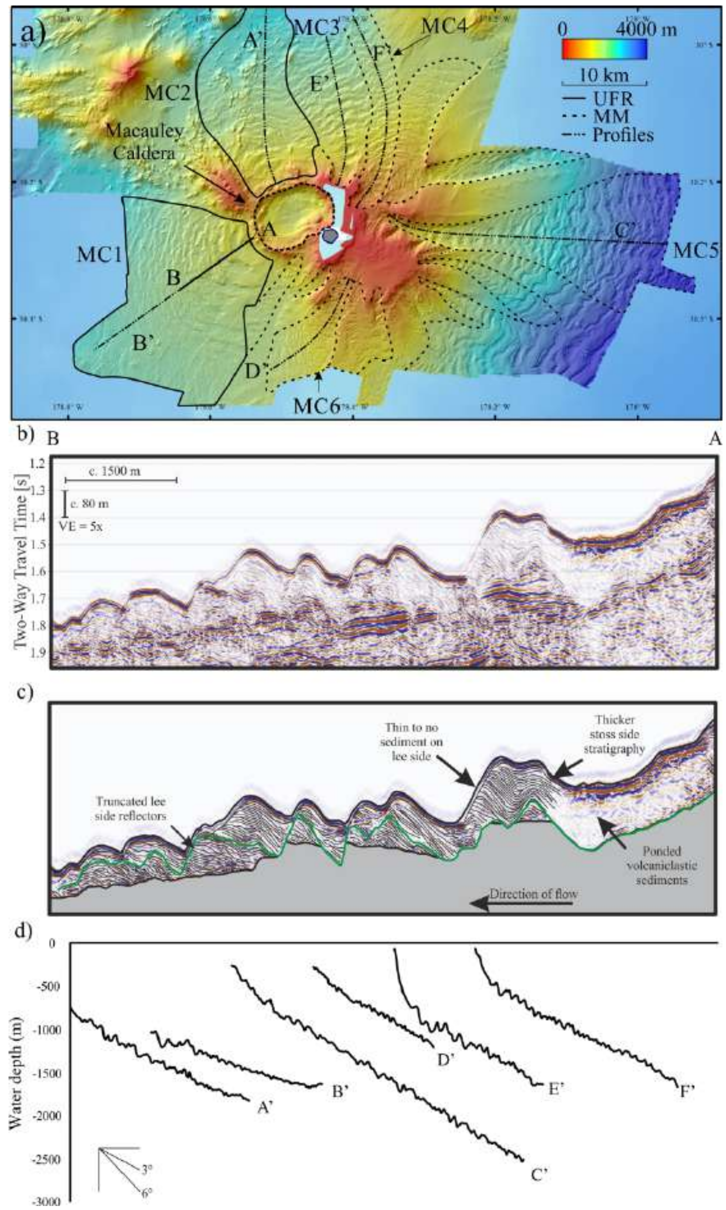

Figure 2. a) Map of bedforms surrounding Macauley Volcano. Bedform fields and associated bathymetric profilers (A' – F') included in Table 1 are indicated. UFR = Upper-Flow Regime. MM = Mass Movement. b) Un-interpreted seismic data perpendicular to the expected direction of flow of an eruption-fed sediment density flow. c) Trace interpretation of seismic reflectors within the bedforms. The green line represents an interpreted unconformity within the bedforms. d) Bathymetric profiles along the centre of the bedform fields described in Table 1.

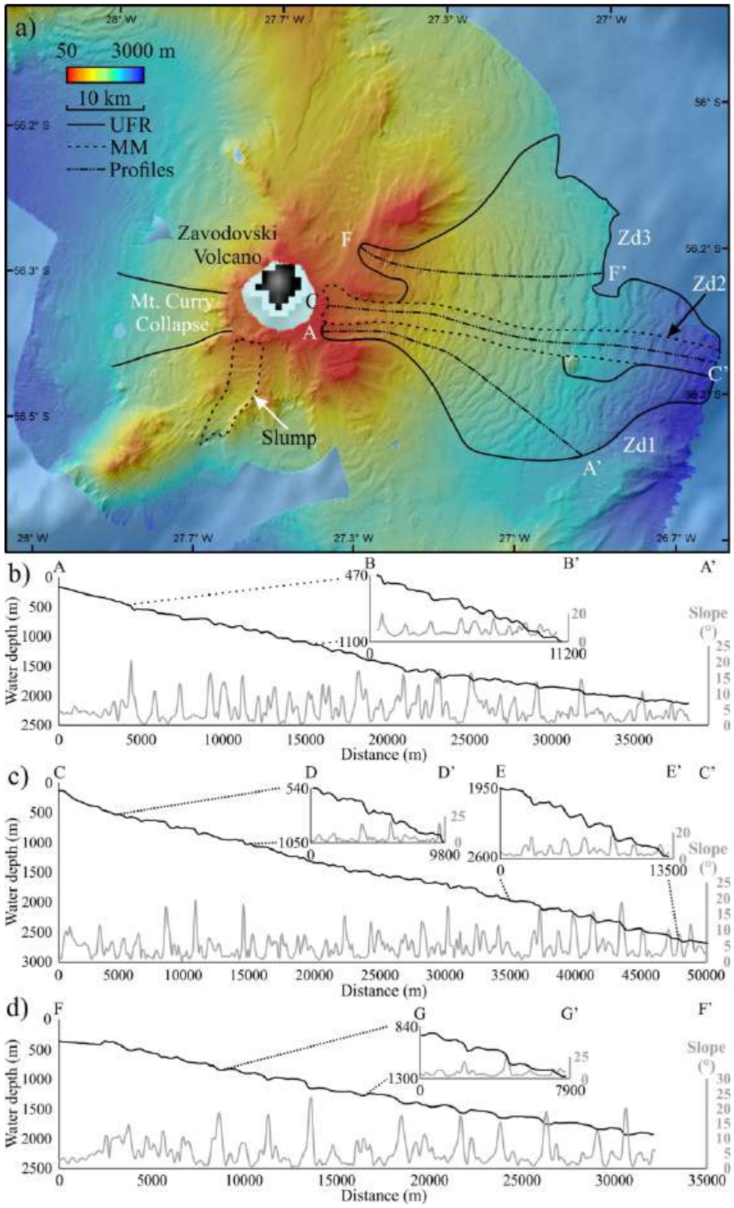

Figure 3. a) Map of bedforms surrounding Zavodovski Volcano. Bedform fields included in Table 1 are indicated. UFR = Upper-Flow Regime. MM = Mass Movements. b – d) Bathymetric profiles and slope gradients along the profiles of the bedform fields identified in a).

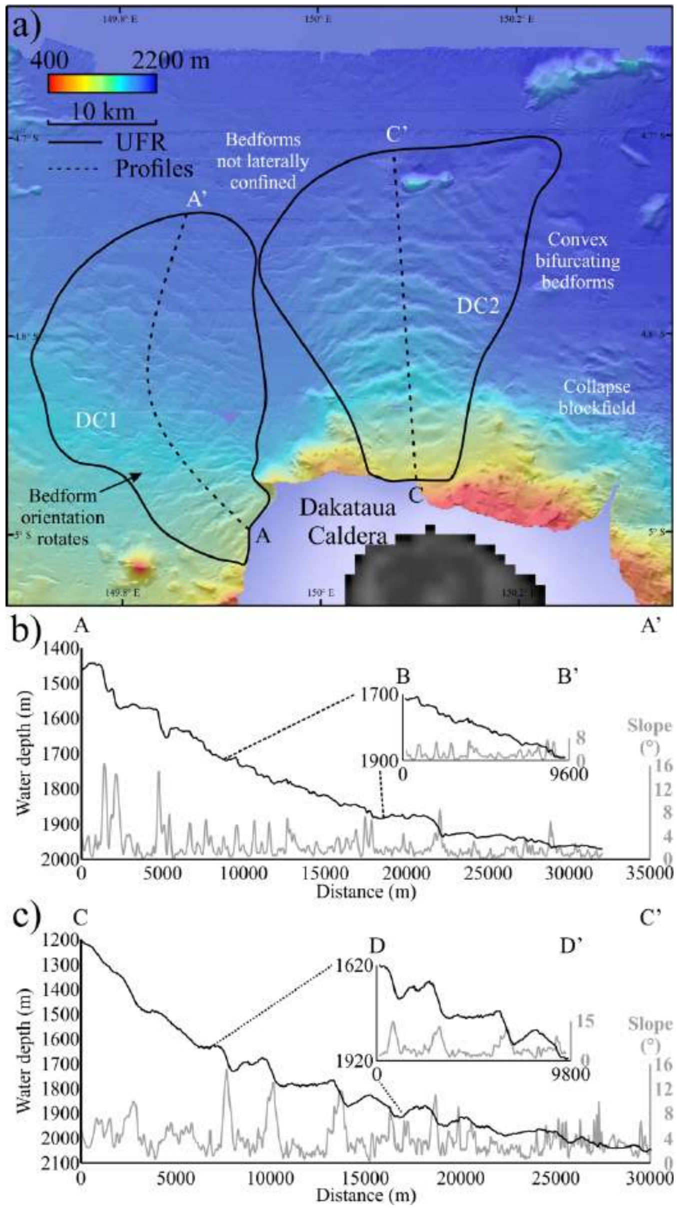

Figure 4. a) Map of bedforms surrounding Dakataua Caldera. Bedform fields included in Table 1 are indicated. UFR = Upper-Flow Regime. b – c) Bathymetric profiles and slope gradients along the profiles of the bedform fields identified in a).

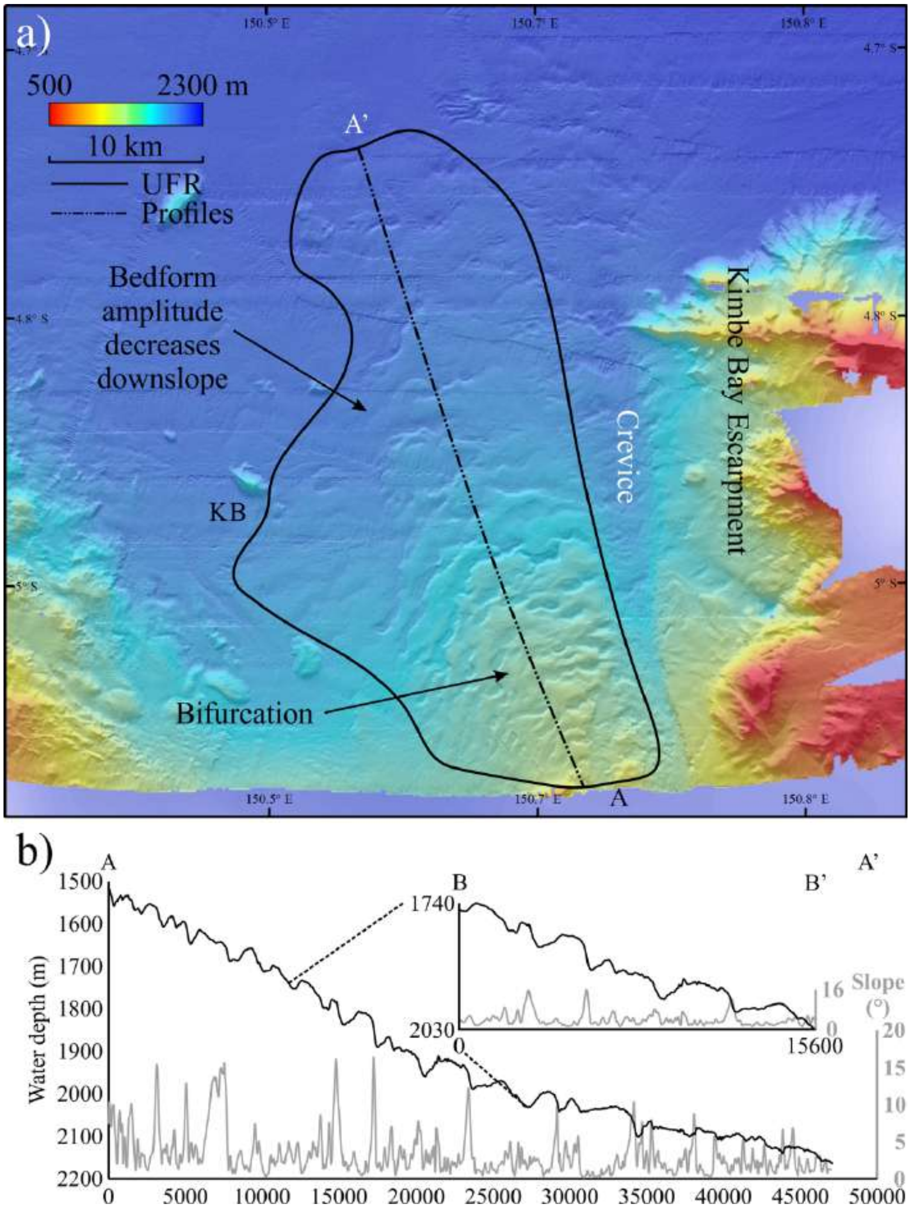

Figure 5. a) Map of bedforms on the seafloor of Kimbe Bay. Bedform field KB is included in Table 1. UFR = Upper-Flow Regime. b) Bathymetric profile and slope gradient along profile A – A' in a).

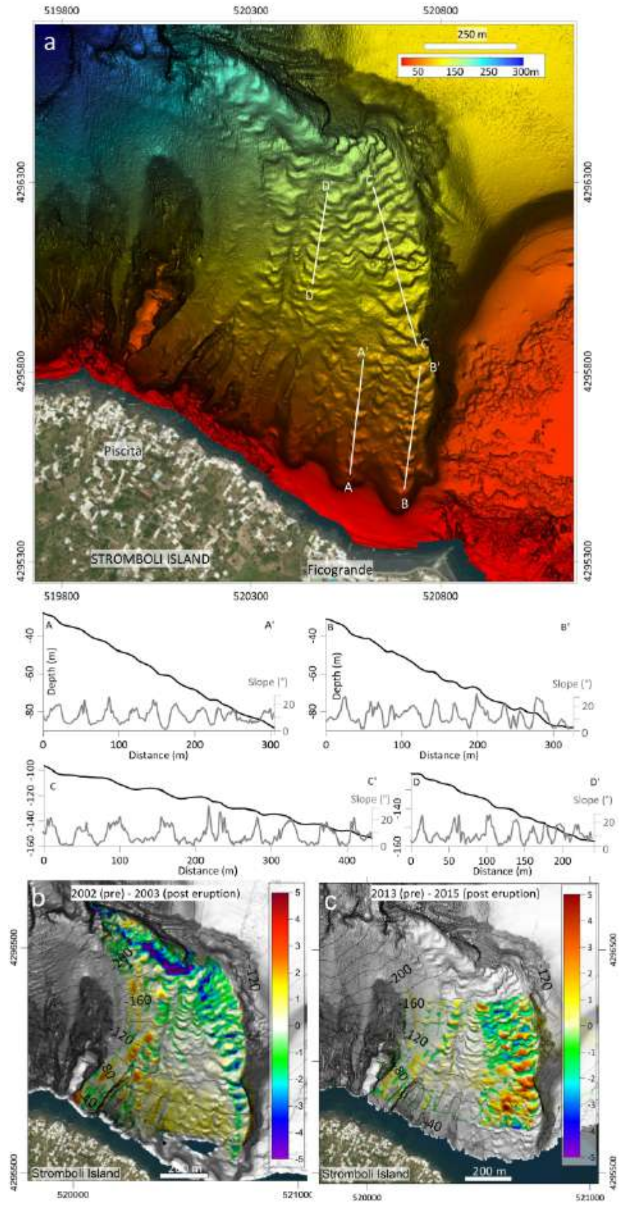

Figure 6 a) Shaded relief map of the Piscità channel, where the bedforms field Str4 (location in Fig. 1 and 1ESM) is recognizable; below, bathymetric sections (dark line) and slope gradients (grey-line) extracted from 2013 DEM are showed. b) Residual map between 2002 and 2003 bathymetries collected before and after the Stromboli 2002 eruption and tsunamigenic landslide, evidencing a main migration of bedforms on the eastern side of the channel. c) Residual map between 2013 and 2015 bathymetries collected before and after the 2014 Stromboli eruption, showing the migration of the bedforms mainly on the eastern side of the channel.

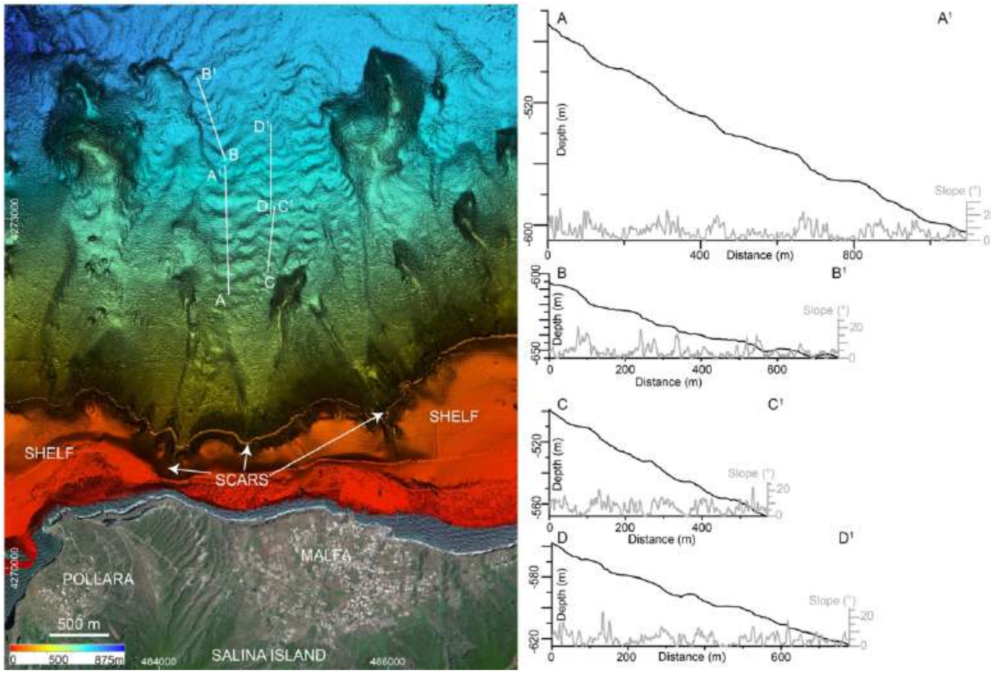

Figure 7 Shaded relief map of the Northern Salina channel, where the bedforms field Sal1 (location in Fig. 1 and 1 ESM) is recognizable; on the right, bathymetric sections (dark line) and slope gradients (grey-line) extracted from the DEM are showed

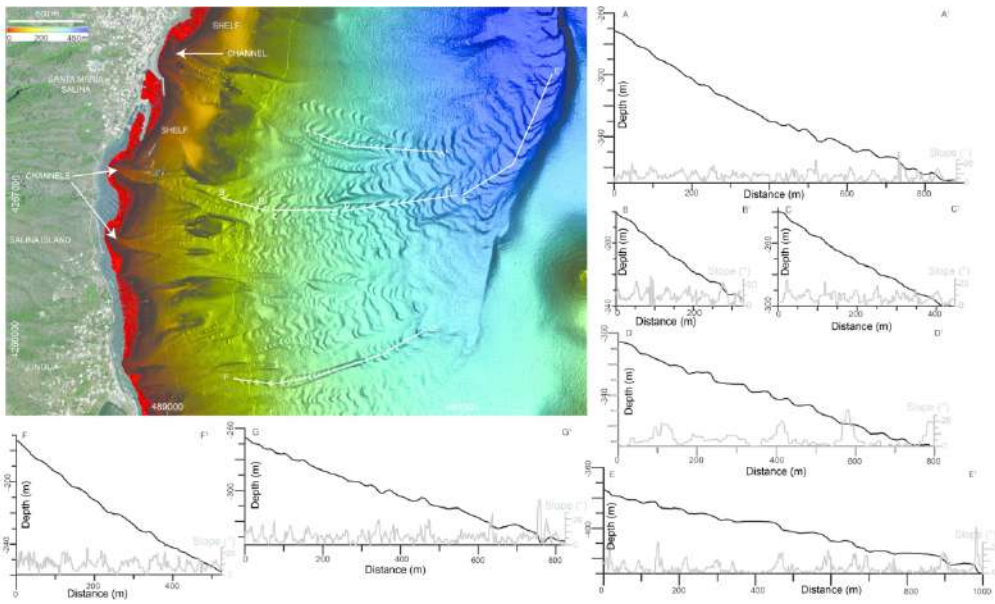

Figure 8 Shaded relief map of the eastern flank of Salina, where the bedforms field Sal2 (location in Fig. 1 and 1 ESM) is recognizable; on the right, bathymetric sections (dark line) and slope gradients (grey-line) extracted from the DEM are showed

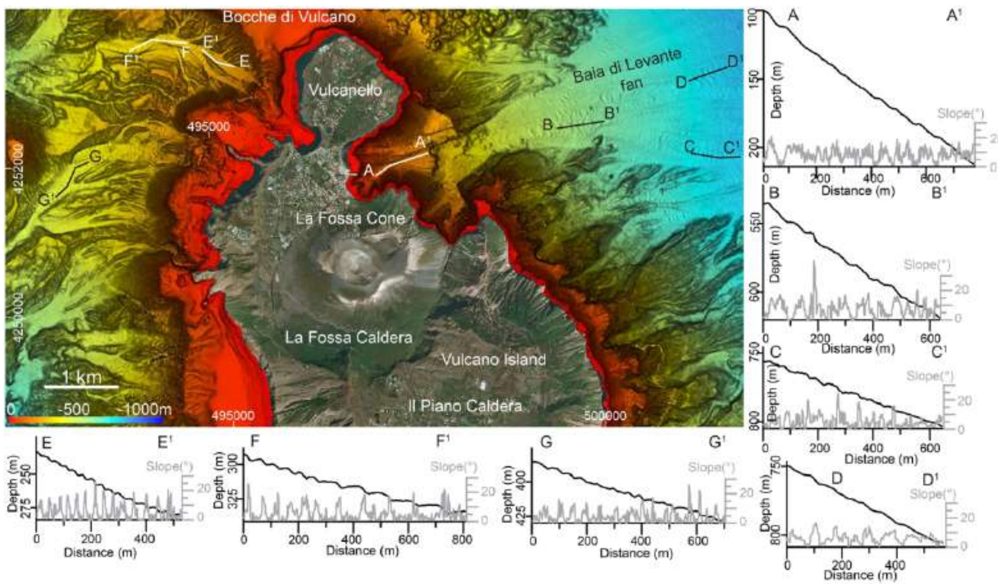

Figure 9 Shaded relief map of the northern flank of Vulcano, where the bedforms fields Vul2 and Vul3 (location in Fig. 1 and 1ESM) are recognizable in the NW and NE flank, respectively; on the right and below, bathymetric sections (dark line) and slope gradients (grey-line) extracted from the DEM are showed.

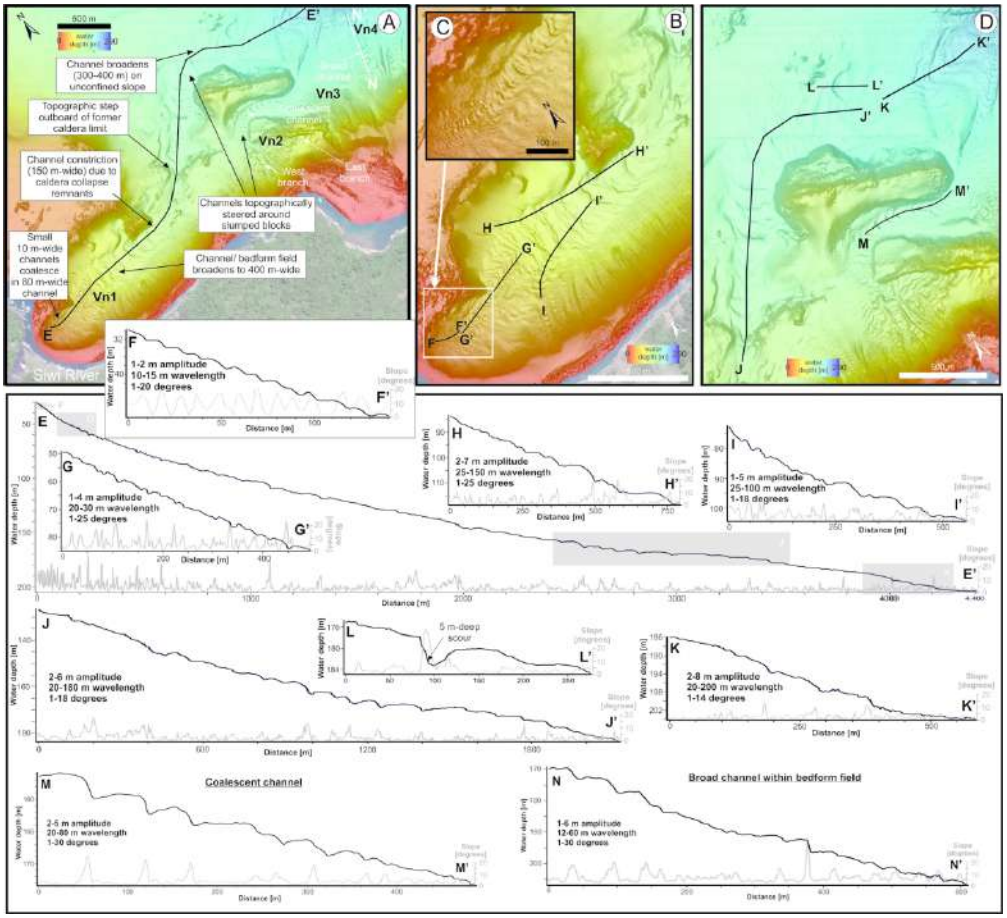

Figure 10 Shaded relief map to illustrate bedform fields offshore Tanna Island, Vanuatu including (A) overview and detailed close-up views (B-D) showing small-scale bedforms. Profiles (F-N) illustrate the variability in scale of bedforms from proximal to distal, as well as in response to topographic changes seaward of the interpreted former caldera collapse (E)

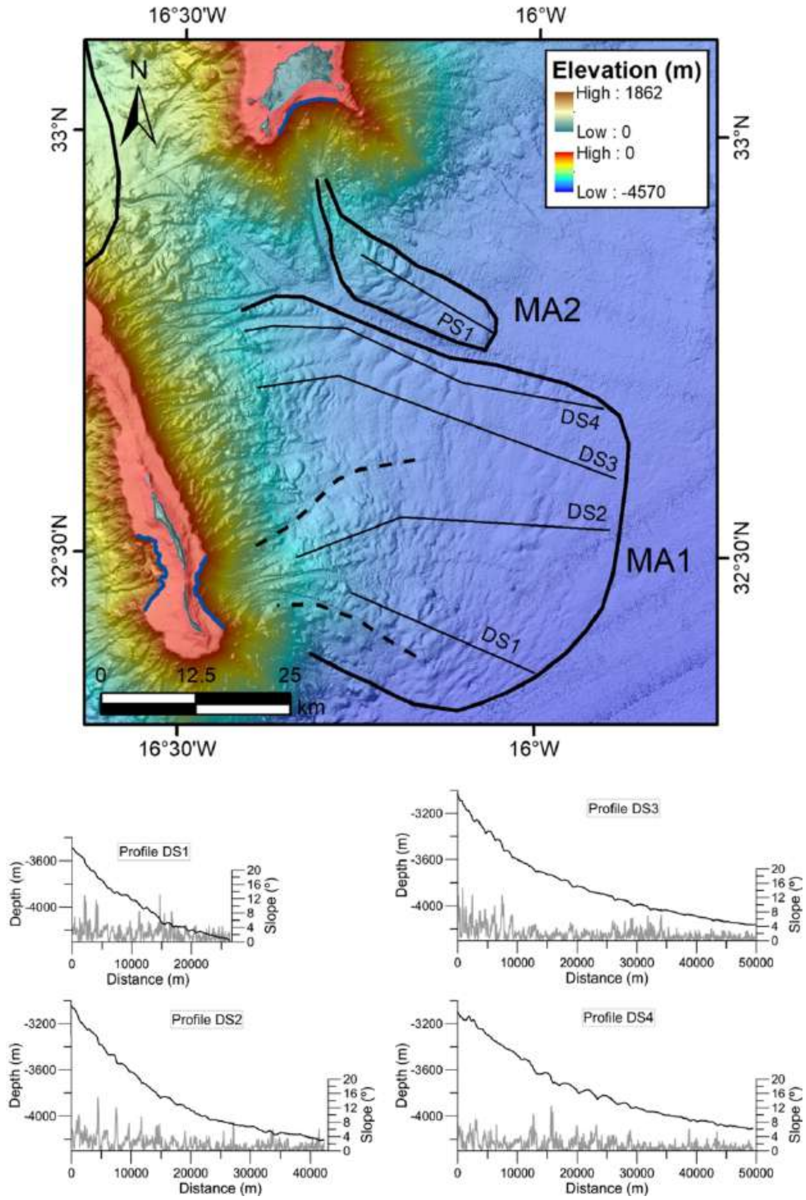

Figure 11 Shaded relief map of the eastern side of Desertas and southern side of Porto Santo where the bedforms MA1 and MA2 were identified. DS1 to DS4 are bathymetric profiles and slope gradients along the profiles of the bedform fields identified in the upper image. Location in Fig. 1 and Fig.2 ESM

170x255mm (300 x 300 DPI)

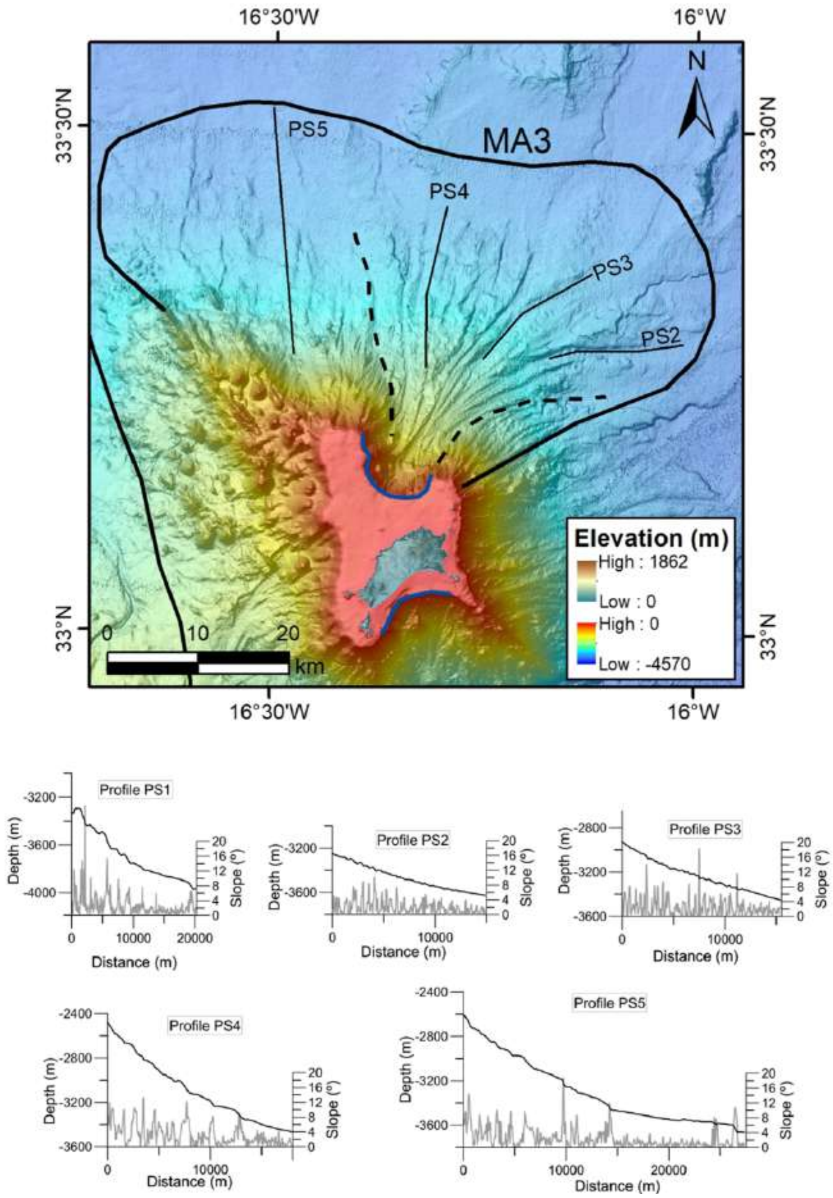

Figure 12 Shaded relief map of the northern side of Porto Santo where the bedforms MA3 were identified. PS1 to PS5 are bathymetric profiles and slope gradients along the profiles of the bedform fields identified in the upper image. Location of PS1 is shown in Fig. 11

170x246mm (300 x 300 DPI)

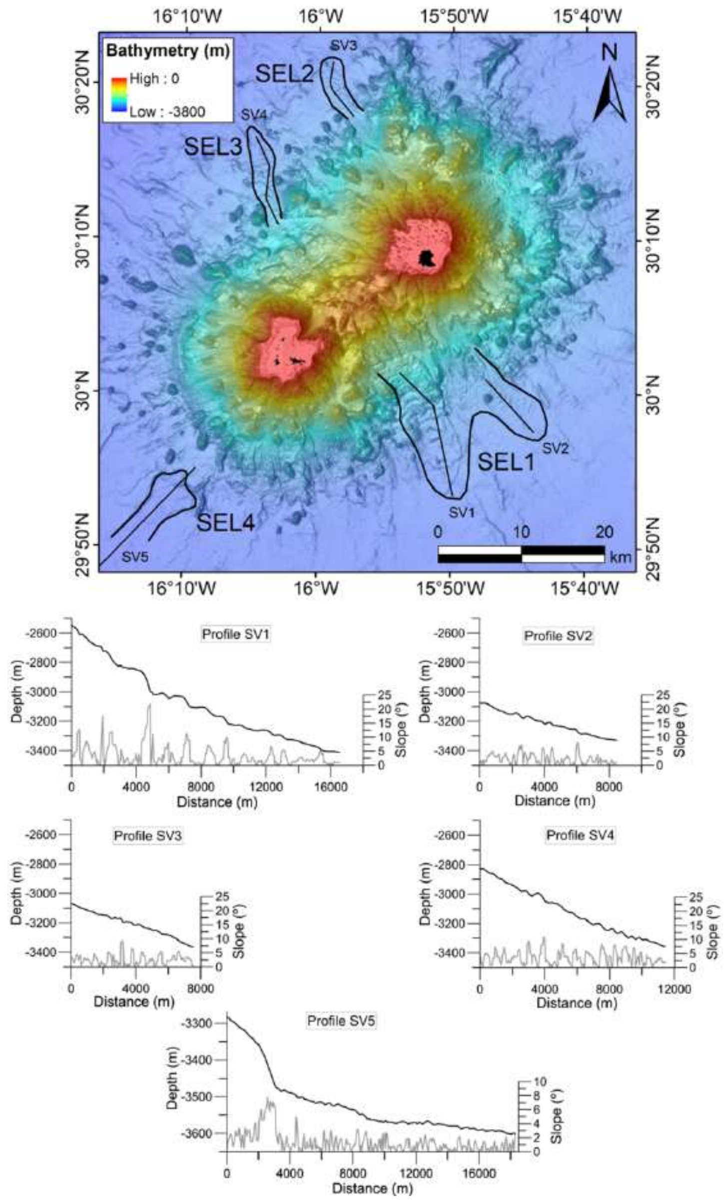

Figure 13 Shaded relief map of Selvagens where the bedforms SEL 1-4 were identified. SV1 to SV5 are bathymetric profiles and slope gradients along the profiles of the bedform fields identified in the upper image.

170x284mm (300 x 300 DPI)

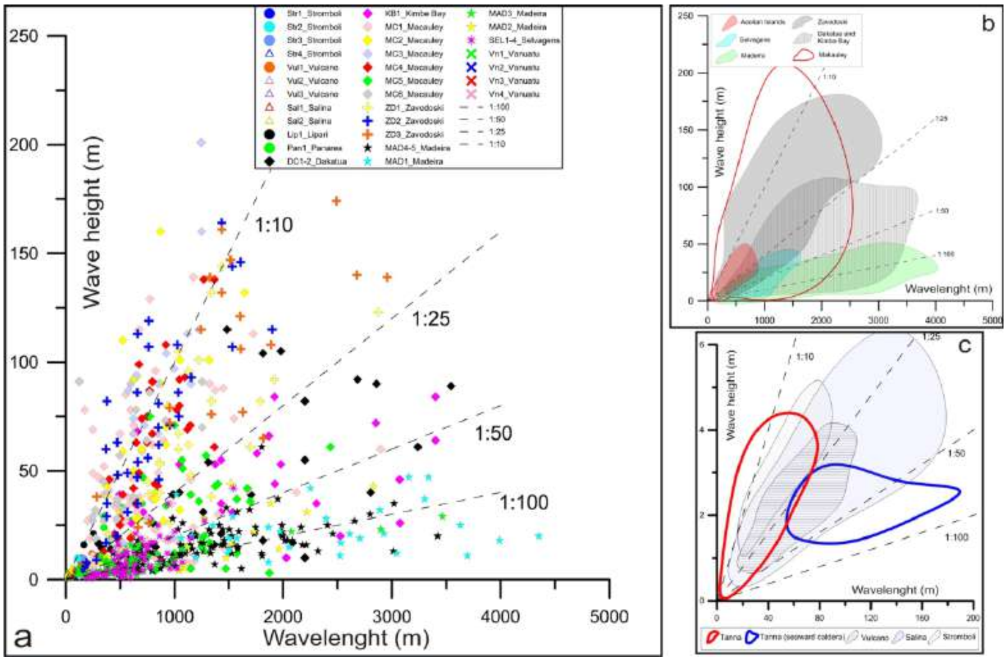

Figure 14 (a) Plot of wave height versus wavelength for all the recognized bedforms. Boundaries of H/L ratio for the large-scale (b) and small-scale (c) bedform fields recognized in the different case-studies. The dashed lines are referred to 1:10, 1:25, 1:50, 1:100 H/L values.

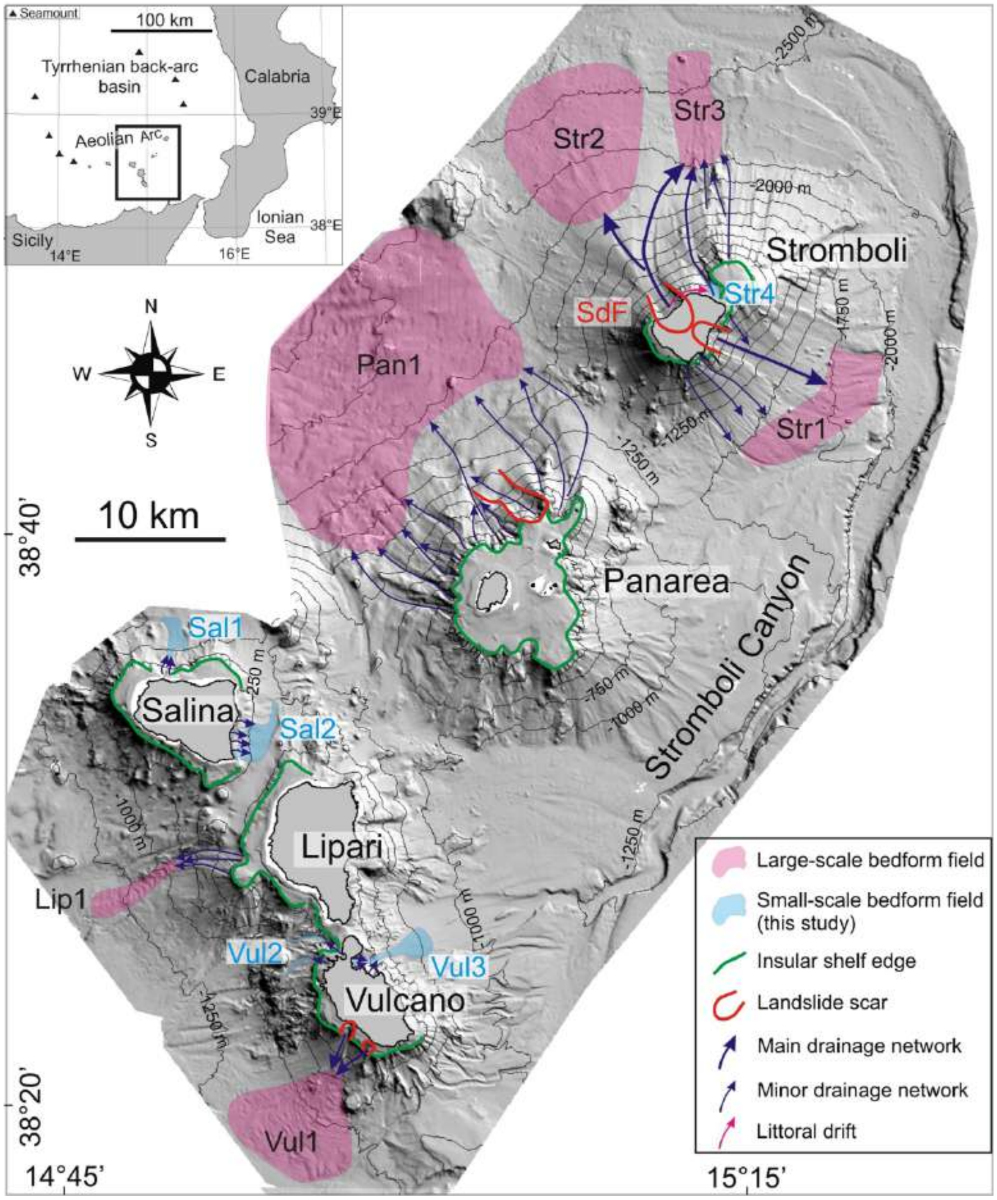

Figure 1 ESM Shaded relief map of the five insular volcanoes making up the central and eastern sectors of the Aeolian Archipelago, with the location of the large-scale (from Casalbore et al., 2014) and small-scale bedform fields described in this study (Figs. 6-9). The main submarine morphological features useful to understand the genesis of the bedforms are also drawn. The inset shows the regional setting of the area, where triangles represent submarine seamounts also belonging to the Aeolian Arc

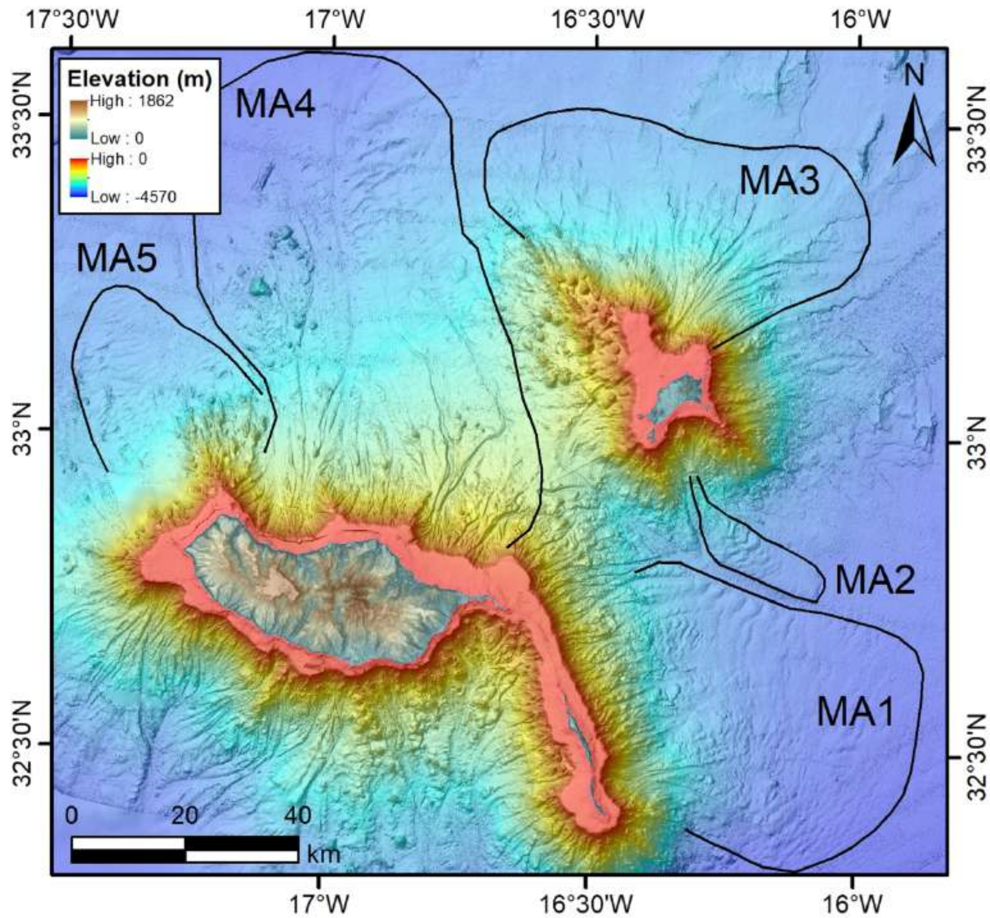

Figure 2 ESM - Shaded relief map of subaerial and submarine part of Madeira, Porto Santo and Desertas Islands with bedform fields identified MA1 to MA5.

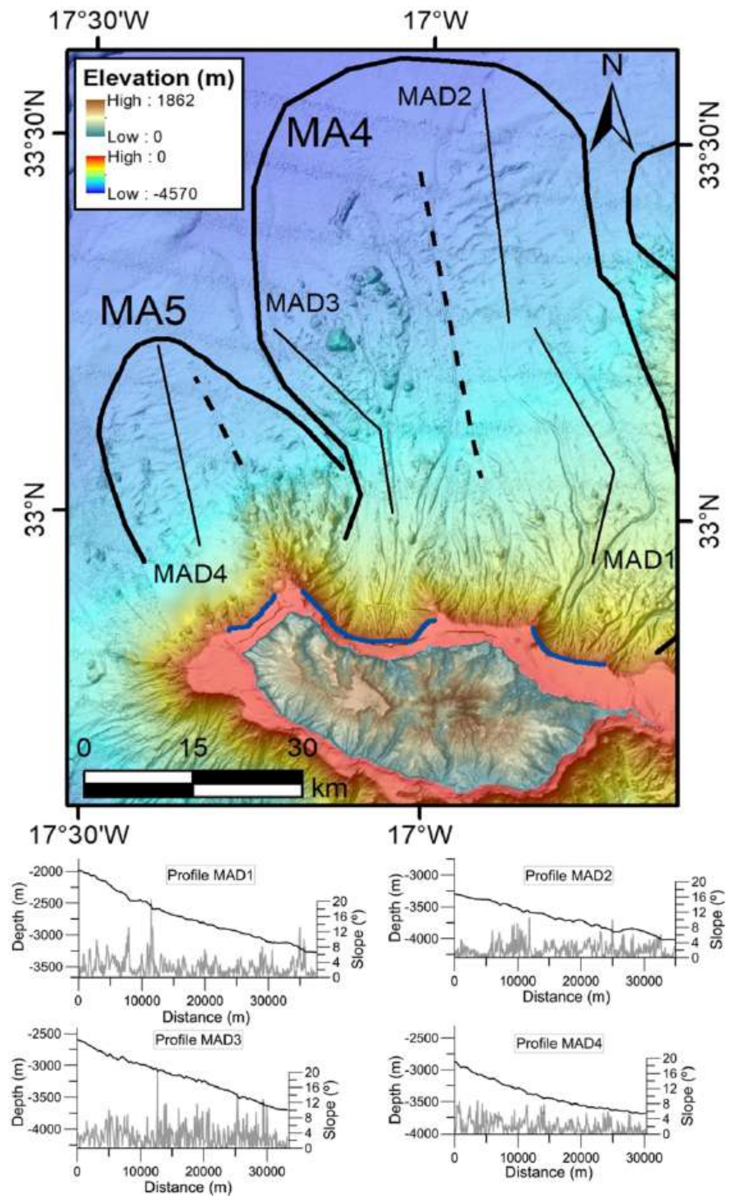

Figure 3 ESM - Shaded relief map of the northern side of Madeira where the bedforms MA4 and MA5 were identified. MAD1 to MAD4 are bathymetric profiles and slope gradients along the profiles of the bedform fields identified in the upper image.

170x281mm (300 x 300 DPI)

Table 1 Main morphometric characteristics of the recognized bedforms. Note that the slope range is referred to maximum and minimum values of the slope gradients measured in the bedforms field by deleting the local effect of the bedforms. L, H and L.E. are wavelength, wave height and lateral extent respectively; min: minimum, max: maximum, med: median. Negative values shown in brackets for stoss-side are referred to the maximum slope gradients measured in the cases where the stoss-side is sloping upslope instead than downslope.

ID*	**Location**	**Area km2**	**Depth range m**	**Slope range °**	**L (min) m**	**L (max) m**	**L (med) m**	**H (min) m**	**H (max) m**	**H (med) m**	**L.E. (min) m**	**L.E. (max) m**	**L.E. (med) m**	**Crestline shape**	**Cross-section**	**Stoss-side (max slope angle) °**	**Lee side (max slope angle) °**
MC1	Macauley	>320	650 - 1700	3.52 -0.99	250	1500	620	5	140	38	7250	27000	17000	convex	Downslope asymmetric	13.7	24.3
MC2	Macauley	220	630 - 1900	5.52 -1.98	220	1650	650	5	160	40	7800	12250	9600	convex	Downslope asymmetric	16.2	22.7
MC3	Macauley	>120	750 - 1650	3.45 -1.95	525	1250	850	17	200	90	2600	9700	7800	cinuous/ linear	Symmetrical	14.6	24
MC4	Macauley	>81	450 - 1650	3.16 -2.66	350	1350	750	13	140	63	2600	4250	3850	cinuous/ linear	Symmetrical	15.6	21.2
MC5	Macauley	>279	600 - 3300	3.36 -3.36	350	2450	1237	5	75	31	800	20100	9100	cinuous	Symmetrical	21.2	28.2
MC6	Macauley	65	350 - 1150	4.59 -2.99	125	1254	475	5	90	37	1900	7400	3200	concave upslope/ linear downslop e	Upslope Asymmetric (upslope) Symmetrical (downslope)	13.3	18.8
Zd1	Zavodovski	368	160 - 2130	4.06 -1.97	380	2800	1037	5	144	54	1450	16500	8200	convex/ linear	Downslope asymmetric	9.9	9.9
Zd2	Zavodovski	186	400 - 2800	3 -2.54	190	1900	663	8	164	63	1700	3150	2100	concave/ linear	Downslope asymmetric Upslope asymmetric	8.1	8.5
Zd3	Zavodovski	>313	370 - 2600	3.96 -2.22	285	2957	1437	24	175	108	2300	12600	10100	linear	Downslope asymmetric	7.84	11.1
DC2	Dakataua Caldera	520	1600 - 2100	1.23 -0.66	820	2860	1898	10	115	40	5900	28500	20200	convex	Downslope asymmetric Upslope asymmetric	5.1	9.9

DC1	Dakataua Caldera	554	1450 - 2000	2.33 -0.3	384	3500	990	5	92	21	6600	19800	15000	sinuous/ linear	Downslope asymmetric Upslope asymmetric	3.66	7.66
KB	Kimbe Bay	700	1500 - 2200	1.1 -0.4	494	3400	1430	7	84	35	7800	21700	13800	convex	Downslope asymmetric Upslope asymmetric	4.77	10.14
Str1	Stromboli SE	15	1500-1700	5 -2	60	400	173	5	20	3.1	70	800	220	sinuous to arcuate	mostly downslope asymmetric	3(-9.3)	13
Str2	Stromboli NW	4	2000–2600	8 -3	60	166	101	2.4	9.7	3.5	100	800	215	sinuous to arcuate	mostly downslope asymmetric	3(-5)	26
Str3	Stromboli N	6	2300-2600	4 -2	97	253	162	3	9.6	4.5	120	800	364	sinuous to arcuate	mostly downslope asymmetric	0.4 (-2.3)	18
Pan1	Panarea NE	100	1800-2500	8 -3	305	800	528	8.8	47	25	1300	2000	1630	sinuous to arcuate	mostly downslope asymmetric	2.6 (-7.3)	17
Vul1	Vulcano SW	20	800-1200	6 -2	122	280	152	4	11.8	7.5	600	2200	1300	sinuous to arcuate	mostly downslope asymmetric	0.6 (-2)	32
Lipa 1	Lipari W	8	870-1260	5 -4	166	414	299	14	21	16	300	700	500	arcuate	mostly downslope asymmetric	4 (-1.8)	32
Str4	Stromboli island (Piscità Channel)	3	30-174	10 -7	20	86	38	1.2	5	2.6	20	122	44	arcuate-crescentic	downslope asymmetric	9(-5)	28

Sal1	Salina Island (N)	3.3	285-677	11 -2.3	44	215	108	1.3	6.2	3.2	60	310	190	arcuate-crescentic	downslope asymmetric	4.2 (-11.5)	29.5
Sal2	Salina Island (E)	3.8	45-430	14 -2	12	153	42	0.2	5.4	1.6	11	184	45	arcuate-crescentic	downslope asymmetric	9	30
Vul2	Vulcano Island (NW)	0.8	200-450	9 -3	30	106	40	1.2	3.8	2	24	160	70	arcuate-crescentic	downslope asymmetric	2.3 (-7)	26
Vul3	Vulcano Island (LFC)	0.2	70-200	9 -7	21	62	35	0.7	2.8	1.3	25	80	50	arcuate	downslope asymmetric	6	15
	Vulcano Island (NE, Baia di Levante fan)	2	500-800	7 -5	36	92	66	1	4	2	70	250	140	sinuous	downslope asymmetric	5 (-1)	18
Vn1	Siwi Channel Bedform field	1.2167 41344	30->208	9 -2	4	180	20	0.3	6	1.85	10	460	240	crescentic to irregular	Asymmetric upslope	4	28
Vn2	Coalesent Channel	0.5344 53774	50->208	9 -1	5	75	18	0.2	8.5	1.3	50	250	150	crescentic to irregular	Asymmetric upslope	4	29
Vn3	Single Channel	0.0719 58029	75-167	15 - 1	13	42	25	1.2	3.8	2.3	50	273	68	crescentic to irregular	Asymmetric upslope	4	24
Vn4	Bedform Channel Field (incl Broad Channel)	0.7037 66529	155->208	15 -1	12	60	30.5	0.5	5.8	1.95	699	1045	755	crescentic to irregular	Asymmetric upslope	5	43
MA1	E Desertas, downslope of landslide	1900	2900-4300	3.8 -0.5	746	3014	1575	5	31	16	26	46	*	sinuous	Change between upslope asymmetric and symmetric	2 (-3.3)	11.6
	E Desertas, downslope of scours			4.7 -0.2	1016	4352	2,154	8	47	20				sinuous	Change between upslope asymmetric and symmetric	0.7 (9.3)	7.9

MA2	S Porto Santo	150	3250-4000	2.3 -0.4	1369	2322	1,548	7	37	23	4	8	*	sinuous	Change between upslope asymmetric and symmetric	*	0
MA3	N Porto Santo, inside channels	1500	2900-3600	3 -0.9	228	983	587	2	16	7	35	70	*	crescentic downslop e	Change between upslope and downslope asymmetric and symmetric	1.8 (-4.7)	21
	N Porto Santo, top of interfluves		2500-3500	5 -0.6	706	3463	1248	4	35	15				crescentic uslope	Change between upslope and downslope asymmetric and symmetric	4.4	12.7
MA4	N of Madeira	3600	2000-4000	3.2 -1.2	388	3421	1095	4	61	16	46	52	*	sinuous	Change between upslope asymmetric and symmetric	1.7 (-9.1)	10.6
MA5	NE of Madeira	600	2900-3600	2.8 -0.6	437	2456	1145	1	24	12	5	30	*	sinuous	Change between upslope asymmetric and symmetric	1.3 (-3.6)	6.7
Sel1	SE of Selvagem Pequena	180	2300-3400	5.3 -1.8	345	1542	857	2	42	13	26	46	*	sinuous	Change between upslope asymmetric and symmetric	4 (-3.7)	12.5
	SE of Selvagem Grande			4.7 -0.2	188	1071	641	1	17	7				sinuous	Change between upslope asymmetric and symmetric	1.4 (-4.8)	7.6

Sel2	NW of Selvagem Grande	20	3000-3400	3.3 -2.6	339	772	627	2	16	6	2	3	*	crescentic upslope/downslope	Change between upslope asymmetric and symmetric	0.5 (-1.5)	8.9
Sel3	NE of Selvagem Pequena	25	2800-3400	3.5 -1.8	439	1026	559	4	35	12	1.5	3	*	crescentic downslope	Change between upslope asymmetric and symmetric	2.1 (-4.6)	9.9
Sel4	SW of Selvagem Pequena	50	3300-3600	1.2 - 0.2	198	784	449	1	10	3	3	4	*	sinuous	Change between upslope and downslope asymmetric and symmetric	0.8 (-2.6)	3.4

Table 2 Summary of grain-size, local boundary conditions and preconditioning and triggering mechanism for the recognized bedforms.

ID*	Location	Grain-size	Morphological setting	Volcanic regime	Meteo-Marine regime	preconditioning and triggers mechanisms
MC1	Macauley	Unknown (only onshore grain sizes available)	Unconfined open slope	Hawaiian - Plinian	Prone to tropical cyclones and storms	Eruption-fed density currents
MC2	Macauley	Unknown (only onshore grain sizes available)	Unconfined open slope	Hawaiian - Plinian	Prone to tropical cyclones and storms	Eruption-fed density currents
MC3	Macauley	Unknown (only onshore grain sizes available)	Confined within sector collapse/Unconfined downslope	Hawaiian - Plinian	Prone to tropical cyclones and storms	Probable slope failure
MC4	Macauley	Unknown (only onshore grain sizes available)	Confined within sector collapse/Unconfined downslope	Hawaiian - Plinian	Prone to tropical cyclones and storms	Probable slope failure
MC5	Macauley	Unknown (only onshore grain sizes available)	Confined within sector collapse	Hawaiian - Plinian	Prone to tropical cyclones and storms	Probable slope failure
MC6	Macauley	Unknown (only onshore grain sizes available)	Confined within sector collapse/Unconfined downslope	Hawaiian - Plinian	Prone to tropical cyclones and storms	Probable slope failure
Zd1	Zavodovski	Unknown	Confined within gully/Unconfined downslope	Strombolian/Vulcanian	Exposed to southern ocean storms and swell	Initial slope failure followed by eruption-fed density currents
Zd2	Zavodovski	Unknown	Confined within gully	Strombolian/Vulcanian	Exposed to southern ocean storms and swell	Probable slope failure
Zd3	Zavodovski	Unknown	Confined within gully/Unconfined downslope	Strombolian/Vulcanian	Exposed to southern ocean storms and swell	Initial slope failure followed by eruption-fed density currents
DC2	Dakataua Caldera	Unknown	Unconfined open slope	Plinian/Sub-plinian/Phreatoplinian	Prone to tropical cyclones and storms with extreme rainfall	Sediment density flow/deformational creep
DC1	Dakataua Caldera	Unknown	Unconfined open slope	Plinian - Vulcanian (Pheatoplinian - Phreatovulcanian)	Prone to tropical cyclones and storms with extreme rainfall	Sediment density flow/deformational creep
KB	Kimbe Bay	Unknown	Unconfined open slope	Plinian/Phreatoplinian	Prone to tropical cyclones and storms with extreme rainfall	Sediment density flow/deformational creep
Str1	Stromboli SE	Backscatter zonation on TOBI mosaic, strong echo on S.B.P.; coarse-sand and gravel at surface	furrows just below a marked decrease of slope gradients	Strombolian activity	microtidal regime, wind from SE waves up to 6 m	sedimentary gravity flows from subareial-submarine depression left by sector collapses
Str2	Stromboli NW	Backscatter zonation on TOBI mosaic, strong echo on S.B.P.; coarse-sand and gravel at surface	turbidite troughs above a volcaniclastic fan due to the emplacement of debris avalanche deposits; associated with decrease of slope gradients	Strombolian activity	microtidal regime, wind from N-NW waves up to 6 m	sedimentary gravity flows from subaerial-submarine depression left by sector collapses

Str3	Stromboli N	Backscatter zonation on TOBI mosaic, strong echo on S.B.P.; coarse-sand and gravel at surface	channel at the base of the saddle between Stromboli and Strombolicchio	Strombolian activity	microtidal regime, wind from SE waves up to 6 m	sedimentary gravity flows from subaerial-submarine depression left by sector collapses and from retrogressive slope failures at the edge of insular shelf
Pan1	Panarea NE	not available	unconfined at the base of the Panarea N flank	lava domes and subordinate explosive activity	microtidal regime, wind from SE waves up to 6 m	channels draining the submarine flanks from retrogressive slope failures at the edge of insular shelf
Vul1	Vulcano SW	coarse-grained volcaniclastic layer in a 1.6 m long core	unconfined on a fan-shaped feature	vulcanian-type activity	microtidal regime, wind from SE waves up to 6 m	sedimentary gravity flows from two wide shallow water scars, partially affecting also the subaerial flank of the edifice
Lipa1	Lipari W	not available	Confined within a straight channelized feature	hydromagmatic and Strombolian activities	microtidal regime, wind from SE waves up to 6 m	retrogressive erosion at the edge of the insular shelf
Str4	Stromboli island (Piscità Channel)	sandy	flat-bottomed channel in the saddle between Stromboli and Strombolicchio	Strombolian to	microtidal regime, wind from SE waves up to 6 m	flat-bottomed channels in a saddle, fed by longshore drift during eruptive crisis
Sal1	Salina Island (N)	sandy	flat-bottomed channel below the shelf edge	subplinian (last eruption 15.6 ka)	microtidal regime, wind from SE waves up to 6 m	retrogressive erosion at the edge of the insular shelf
Sal2	Salina Island (E)	sandy	channels-fan/large channel	Strombolian to subplinian (last eruption 13 ka)	microtidal regime, wind from SE waves up to 6 m	channels morphologically linked to steep creeks onland draining pyroclastic rocks
Vul2	Vulcano Island (NW)	sandy	flat-bottomed channel	vulcanian-type activity	microtidal regime, wind from SE waves up to 6 m	retrogressive erosion at the saddle between Vulcano and Lipari and Vulcanello isthmus
Vul3	Vulcano Island (LFC)	sandy	gullies within La Fossa Caldera	vulcanian-type activity	microtidal regime, wind from SE waves up to 6 m	sedimentary density flows flow from the dismantling of La Fossa Caldera infilling
	Vulcano Island (NE, Baia di Levante fan)	sandy	fan-shaped feature below La Fossa Caldera	vulcanian-type activity	microtidal regime, wind from SE waves up to 6 m	sedimentary density flows flow from the dismantling of La Fossa Caldera infilling
Vn1	Siwi Channel Bedform field	Fine to medium sand (based on ROV surface sampling)	Within and on outer edge of caldera collapse, which has defined location of channels	Strombolian	Prone to significant tropical cyclones and storms with extreme rainfall, which can trigger elevated river discharges (>1000 m3/s). This partiuclarl bedform field may be linked to a volcanic lake outburst flood in AD 2000.	sedimentary density flows

Vn2	Coalesent Channel	Fine to medium sand (based on ROV surface sampling)	Within and on outer edge of caldera collapse, which has defined location of channels	Strombolian	Prone to significant tropical cyclones and storms with extreme rainfall, which can trigger elevated river discharges (>1000 m3/s).	sedimentary density flows
Vn3	Single Channel	Fine to medium sand (inferred from ROV sampling in nearby areas)	Within and on outer edge of caldera collapse, which has defined location of channels	Strombolian	Prone to significant tropical cyclones and storms with extreme rainfall, which can trigger elevated river discharges (>1000 m3/s).	sedimentary density flows
Vn4	Bedform Channel Field (incl Broad Channel)	Fine to medium sand (inferred from ROV sampling in nearby areas)	Immediately seaward of caldera collapse	Strombolian	Prone to significant tropical cyclones and storms with extreme rainfall, which can trigger elevated river discharges (>1000 m3/s).	sedimentary density flows
MA1	E Desertas, downslope of landslide	No information	Landslide scar upslope	Mostly Hawaian activity	microtidal regime, wind from SE waves up to 1.2 m	sedimentary density flows
	E Desertas, downslope of scours	No information	Channels upslope, located where gradients decrease to less than 5º	Mostly Hawaian activity	microtidal regime, wind from SE waves up to 1.2 m	Big scar uplsope, might be landslide derived
MA2	S Porto Santo	No information	Landslide scar upslope	Mostly Hawaian activity	microtidal regime, wind from SE waves up to 1.2 m	Big scar uplsope, might be landslide derived
MA3	N Porto Santo, inside channels	Lee side shows high backscatter	Inside channels	Mostly Hawaian activity	microtidal regime, wind from NW waves up to 5.2 m	sedimentary density flows
	N Porto Santo, top of interfluves	Lee side shows high backscatter	Landslide scar upslope	Mostly Hawaian activity	microtidal regime, wind from NW waves up to 5.2 m	Big scar uplsope, might be landslide derived
MA4	N of Madeira	No information	Landslide scar upslope	Mostly Hawaian activity	microtidal regime, wind from NW waves up to 5.2 m	Big scar uplsope, might be landslide derived
MA5	NE of Madeira	Lee side shows high backscatter	Landslide scar upslope	Mostly Hawaian activity	microtidal regime, wind from NW waves up to 5.2 m	Big scar uplsope, might be landslide derived

Sel1	SE of Selvagem Pequena	No information	Downslope of submarine ridge linking the two islans	Mostly Hawaian activity	microtidal regime, wind from SE waves less than 1 m	sedimentary density flows from volcanic activity
	SE of Selvagem Grande	No information	Channels upslope, located where gradients decrease to less than 5º	Mostly Hawaian activity	microtidal regime, wind from SE waves less than 1 m	sedimentary density flows from erosion of channel
Sel2	NW of Selvagem Grande	Lee side shows high backscatter	Channels upslope, located where gradients decrease to less than 5º	Mostly Hawaian activity	microtidal regime, wind from NE waves up to 4.3 m	sedimentary density flows from erosion of channel
Sel3	NE of Selvagem Pequena	Lee side shows high backscatter	Channels upslope, located where gradients decrease to less than 5º	Mostly Hawaian activity	microtidal regime, wind from NE waves up to 4.3 m	sedimentary density flows from erosion of channel
Sel4	SW of Selvagem Pequena	No information	Scour scar upslope	Mostly Hawaian activity	microtidal regime, wind from NE waves up to 4.3 m	Scour uplsope, sediment density flows erosion of scour

DATA

Macauley Volcano

Multibeam echo-sounder data were acquired around Macauley Volcano in May 2007 onboard RV *Tangaroa* (TAN0706) using a Kongsberg EM300 30 kHz echo-sounder. Data were gridded to a 25 m cell size with a vertical resolution <1% of water depth. These data were supplemented by multichannel seismic data collected using a GI airgun source with a 48 channel streamer. A seismic velocity of 1600 m/s was used to convert two way travel time to depth.

Zavodovski Volcano

Multibeam echo-sounder data were acquired around Zavodovski Volcano in 2007 onboard RRS James Clark Ross (JR168) using a Simrad EM120 12 kHz echo-sounder. Data were gridded to a 100 m cell size with a vertical resolution of 0.5 m or 0.2% of water depth root mean square depending on which is greatest (Tate and Leat, 2007; Leat et al., 2010). Sub-bottom profiler data were collected on a subsequent cruise of the RRS James Clark Ross (JR206) in 2010 using a hull-mounted Simrad TOPAS PS018 profiler (see Leat et al., 2010 for full details).

Dakataua Caldera and Kimbe Bay

Multibeam echo-sounder data were acquired around New Britain, Papua New Guinea in 2004 onboard RV Kilo Moana (KM0419) using a hull-mounted Simrad EM120 12 kHz echo-sounder. Data were gridded at 50 m (Hoffmann et al., 2008). Sub-bottom profiler data were collected using an Edgetech 1 – 6 kHz profiler (see Hoffmann et al., 2008 for full details).

Aeolian Archipelago

Multibeam data were collected during several oceanographic cruises around the Aeolian Archipelago since 2002 on board the R/V Thetis, Minerva1, Urania (belonging to the National Research Council) and small boats for coastal surveys. The Digital Elevation Model (DEM) of the volcanic edifices was realized by merging multiple dataset acquired with high resolution multibeam systems working at different frequencies (from 50 to 455 kHz), allowing the optimal resolution for each bathymetric interval. All data were DGPS- or RTK-positioned and processed with dedicated hydrographic software (for details on data processing refer to Romagnoli et al., 2013, Bosman et al., 2014 and 2015). Sounding density and resolution decrease from the coastal sector towards the submarine base of volcanic edifices, consequently DEMs with cell size varying from 0.5 m in shallow water (<50 m water depth, wd hereafter) up to 25 m in deep water (down to 2900 m wd) were produced. DEMs used for time-lapse bathymetric comparison at Piscità Channel (Stromboli) were acquired in 2002, 2003, 2013 and 2015, and gridded at 1 m up to 380 m water depth. Ancillary data used for bedforms interpretations are deep-towed, long-range side scan sonar data (TOBI working at a frequency of 30 kHz), seismic profiles acquired with 3.5 kHz SBP and 1 kJ Sparker, and seafloor sampling already presented in Romagnoli et al. (2009a and b) and Casalbore et al. (2010 and 2014).

Tanna Island

A multibeam survey was performed by EGS Survey on behalf of the UK Hydrographic Office in March 2017. The survey covers an area of approximately 6.5 km x 3.2 km, and extends from the coastline to 292 m water depth (Fig. 2A). Multibeam bathymetry data were acquired using a Kongsberg EM2040 system (200 to 400 kHz range) and processed into 2 m x 2 m bins; hence features smaller than 2 m across cannot be resolved. Offshore sediment sampling was performed using a two-disc grabber-cup (10 cm3) mounted on a small portable Deep Trekker DTG2 Remotely Operated Vehicle (ROV) equipped with an additional high resolution camera (GoPro HERO4 silver) and deployed from the MV Escape (a 12.9 m catamaran) in October 2017. Offshore sediment samples were targeted within a submarine channel (three locations). Onshore sediment samples were hand-excavated from five locations in the Siwi River during the same survey in October 2017. Grain size analysis followed the procedures in Rothwell et al. (2006). Sediment was sieved at 2 mm to remove rare over-sized particles then three aliquots of each sub-sample were taken for measuring grain size. Aliquot samples (1 g) were dispersed in 30 ml 0.05% sodium hexametaphosphate solution and shaken for 24 hours. Dispersed aliquots were analysed using a Malvern Mastersizer 2000 using laser diffraction of suspended sediment grains (10,000 counts) to measure grain size distributions. Grain size distributions were measured three times per aliquot. Aliquots showed intra-sample variations of <3%. Standard reference materials showed intra-sample variations of up to 3% and accuracy towards reference values of 1.5%. Scanning Electron Microscopy (SEM) was performed using a Hitachi TM-1000 Microscope at the British Ocean Sediment Core Research Facility (BOSCORF) on selected samples to investigate micro-textural properties of the sediments.

Madeira Archipelago

Multibeam data were collected by the Portuguese Hydrographic Institute (IH) during several oceanographic cruises around the archipelago since 2005 on board of the R/V's Gago Coutinho and D. Carlos I, and small boats for coastal surveys. Multibeam systems included Kongsberg EM120 (12 kHz), EM710 (70-100 kHz) and EM3002 (300 kHz). The positioning of the hydrographic data was guaranteed through inertial sensors and Global Navigation Satellite Systems in differential mode and processed using the Combined Uncertainty and Bathymetry Estimator algorithm (Calder and Mayer, 2003) implemented in Caris HIPS & SIPS software and by manual editing of data to remove false soundings. The resolution of the digital elevation models were produced with cell-size varying from 2 m in shallower areas to 128 m for deeper areas (Quartau et al., 2018; Santos et al., 2019).

Large-scale bedforms from the Aeolian Islands

At Stromboli, large-scale bedforms were found at depths of 1500-2600 m along the N, NW and E flanks of the edifice (Str1, Str2 and Str3 in Fig. 1 ESM) on slope gradients of 2°-8°, mostly downslope of large subaerial-submarine depression left by sector collapses (Romagnoli et al., 2009a and b). Bedforms have wavelength of 60-400 m and wave height of 2.4-20 m (Table 1) and they generally display sinuous/arcuate crestlines and downslope asymmetry on cross-sections. Bedforms sometimes tend to increase their wave dimension downslope, where slope gradients decrease, and the seafloor morphology is more regular and flatter. They are easily detectable on deep-towed side scan sonar data, where low-backscatter tones occur on the stoss side and high-backscatter tones on the crest-line and lee side. On Sub-bottom profiles, bedforms are characterized by a very strong echo and lack of seismic penetration in agreement with the coarse-sand and gravel recovered from seafloor sampling. The bedforms are mainly confined within the thalweg of shallow erosive features and occur in correspondence of a marked decrease in slope gradients. Based on this evidence, the genesis of these bedforms has been related to the frequent occurrence of sedimentary gravity flows generated within the large sector collapse depression that collects and act as a main pathway for the fast transport of volcaniclastic material offshore, especially when this is fed by persistent Strombolian volcanic activity (Rosi et al., 2000), as at the present-day Sciara del Fuoco (SdF in Fig. 1 ESM) on the NW flank.

At Panarea, a large bedform field was identified on the northern flank of Panarea between 1800 and 2500 m water depth on slope gradients of 3°-8° (Pan1 in Fig. 1ESM). Bedforms have wavelengths of 300–1000 m and wave heights of 8–50 m, generally increasing their size downslope. They have sinuous or arcuate shape on plan-view and mostly downslope asymmetric in cross-section, with steep (up to 32°) lee sides. The genesis of such bedforms has been associated with the spreading of unconfined sedimentary gravity flows coming from the radial network of channels draining the steep submarine flanks of Panarea. These channels have their headwall at the edge of the insular shelf surrounding the Panarea island, that is almost totally smoothed by a thick (locally up to 200 m) volcaniclastic sedimentation (Chiocci and Romagnoli, 2004).

At Lipari, a coaxial train of bedforms is recognizable within a straight and up to 700 m-wide channel on the western flank at depth between 870 and 1260 m on slope gradients of 4° (Lip1 in Fig. 1 ESM). The bedforms have wavelength of 160–420 m and wave height of 14–25 m. They have arcuate/crescent-shaped crestlines and are downslope asymmetric in cross-section. The origin of such bedforms is more controversial, because they could be interpreted both as retrogressive failures or more likely as upper-flow regime sediment waves formed by sedimentary gravity flows, whose morphological trace is the network of narrow gullies that indent the outer edge of the insular shelf cutting the summit of the eccentric submarine volcanic center of Banco del Bagno (Fig. 1).

At Vulcano, large-scale bedforms occur at depths of 800-1200 m in the middle/lower part of a fan-shaped feature characterized by slope gradients of 2°-6° (Vul1 in Fig. 1 ESM; Romagnoli et al., 2013b). Locally, bedforms develop as coaxial trains elongated along the maximum slope, defining a series of proto-channels on the fan surface. The bedforms have wavelengths of 100-300 m and wave-heights of 4-20 m. They have sinuous crestlines and are mostly downslope asymmetric on cross-section, with lee side up to 30° steep. On Sparker profile (Romagnoli et al., 2013b), the bedforms develop on the top of an acoustically semi-transparent seismic unit; even if diffraction hyperbolae partially mask the surface reflectors, bedforms are made by high-amplitude reflectors, with an overall upslope migration. The genesis of such bedforms can be referred to repeated sedimentary gravity flows sourced from two large coastal scars that deeply indent the insular shelf edge in the southwest part of the island, also matching a large a large embayment in the coast (Romagnoli et al., 2013). Such interpretation is supported by the recognition of different normal-graded volcaniclastic deposits in a 1.6 m long core recovered from the bedforms fields (Romagnoli et al., 2013b). Differently, we tend to discard an origin from pyroclastic flows emplaced by the 100-ka old Il Piano Caldera, because no typical caldera-forming deposits are recognized at Vulcano (Lucchi et al., 2013). It is also noteworthy that the bedforms could have been favored by an uneven paleo-topography corresponding to the top of the mass-transport deposit recognized on seismic profile.

Large-scale bedforms from the N and NW flanks of Madeira Archipelago

North of Madeira: A large bedform field (Bf4) with ~3600 km^2, occurs north of Madeira at 2000-4000 m depth. This area is mostly dominated by deposits from debris avalanches, which in turn are very incised by channels (Quartau et al., 2018). The shallower bedforms (2000-3600 m depth) are very irregular in wavelength and plan view and can be found mostly in the interfluve areas (see profiles MAD1 and MAD3 in Fig. 4). There are also bedforms on a deeper area (3300-4000 m depth) not incised by channels (see profile MAD2). The waves change between upslope asymmetric and symmetric in cross-section and sinuous in plan-view. They are 4-62 m in height and 388-3421 in wavelength. The debris avalanche deposits in this area were linked by Quartau et al. (2018) to two big amphitheater scars on the shelf edge of ~20 km (drawn by blue lines in Fig. 4). The bedforms in the interfluves are probably related to sediment density flows that overtop debris avalanches as the ones SE of Desertas, SE and NE of Porto Santo. The deeper bedforms are just downslope of the end of two ~50 km long channels and in this area the slope gradient is more or less constant (~1º). Therefore, these deeper bedforms were not likely formed by the gradient change but rather by unconfined sediment density flows due to spreading of the sediments over wide areas as they leave the channels.

NW of Madeira: A small bedform field (Bf5) with ~600 km^2, occurs NE of Madeira at 2900-3600 m depth (see Fig. 4). The shallower depth of these bedforms corresponds to the area where the large gradient change (from 30º to less than 5º) occurs. The waves (see profile MAD4 and MAD3 in Fig. 4) are mostly upslope asymmetric (although some are symmetric) in cross-section and sinuous in plan-view. They are 1-24 m in height and 437-2456 in wavelength. The bedforms occur downslope of a less-well defined amphitheater scar at the shelf edge (drawn by a blue line in Fig. 4) mimicked by the coastline with cliffs up to 500 m. Hence, they could be related to the formation of the debris avalanche deposits of this huge landslide. However, the bedforms also begin at the large gradient transition and could also be related to unconfined sediment density flows. A third hypothesis for their origin could be pyroclastic flows from explosive volcanism of the volcanic ridge that extends around 14 km from the NW tip of the shelf edge and covers a relatively large area (~225 km^2).